Simulation of 3D hydrothermal circulation and application to faulted oceanic ridge systems

Ingrid Kristine Jacobsen

Master thesis in Applied and Computational Mathematics,

Department of Mathematics, University of Bergen

June 2022

Acknowledgements

First, I would like to give a huge thank you to my supervisors Omar Duran and Inga Berre. I am forever grateful for the guidance you have provided and the interesting discussions we have had throughout the work of this master thesis. A special thank you will be extended towards my main supervisor, Omar, for always being so patient and willing to help in both long and short periods of time. I really appreciate your supervision and everything I have learnt from you. I would like to thank you, Inga, for getting me interested and invested in this field of research in the first place. Your expertise has been a great source for motivation and encouragement in the work of this thesis. This would not have been such a good master experience without the two of you, so thank you again!

I also want to thank all my friends for being there for fun conversations and discussions, both in our spare time and during some (way too long) lunches. Those have been a great contrast to the work with this thesis, and these past six months would not have been the same without you. So, thank you, all of you!

A final gratitude will be extended towards my family and my better half, Vilde. All of you have been an invaluable and great support which I highly appreciate. Thank you for your support and for reminding me that there are other things to do than just working.

Abstract

Hydrothermal circulation in locations close to oceanic spreading ridges gives dissolved minerals from the crustal rock a chance to reach the seafloor. Temperature is increasing steadily with depth, heating water which resides within the permeable and faulted crust. At sufficient permeability, this causes the fluid to rise due to a lower density, allowing for dissolved minerals from the surrounding rock to be convected upwards.

Natural convection in porous media heated from below is a thoroughly studied field, and we have studied this for faulted domains with parameters representative for the subseafloor. We have numerically solved the fully coupled conservation equations for fluid volume and energy with code based on tools from the open-source Python framework PorePy. The 3D domain where the equations have been solved are represented as a mixed-dimensional domain, where the porous rock, faults and fault intersections are treated as individual subdomains. The key concept behind a mixed-dimensional domain is that the different subdomains have different dimensions, meaning that within a 3D rock, the faults will be 2D, and fault intersections are 1D. Verification of the code has been done by confirming consistency in solutions with different initial conditions, and by numerical benchmarking against theoretical critical Rayleigh numbers for three different 3D domains.

For fluid flow in faulted domains, it is expected that the fluid mainly flows through the faults as they are more permeable than the surrounding rock, and this is confirmed by the simulations. The results also present clearly how convection patterns are greatly impacted by different permeability ratios between the faults and the host rock, which may motivate further research considering layered or anisotropic porous media. The presence of faults is shown important for occurrence of hydrothermal convection in locations containing less permeable rock. Hence, the thesis illustrate how simulations can aid in understanding of governing processes for fluid circulation and transport of minerals in the subseafloor.

Table of Contents

List of Symbols v

List of Figures vi

List of Tables ix

Outline 1

1 Introduction 2

2 Porous Media and Fluid Characteristics 6

2.1 Properties of Porous Media 6

2.2 Properties of the Fluid 7

2.3 Porous Media and Fluid Properties 8

3 Governing Equations 9

3.1 Flow and Heat Transfer in Porous Media 9

3.1.1 Darcy's Law and Volume Conservation 10

3.1.2 Heat Flux and Energy Conservation Equation 13

3.2 Flow and Heat Transfer in Faulted Porous Media 14

3.2.1 Geometric Representation of Faulted Porous Media 14

3.2.2 Conservation Equations for Flow in a Faulted Domain 15

3.2.3 Coupling Conditions 16

3.3 Model Equations 17

4 Numerical methods 20

4.1 Finite Volume Methods and Flux Approximation 20

4.1.1 Multi-Point Flux Approximation 21

4.1.2 Upwind Scheme for the Advection Term 22

4.2 Discretization in Time 23

4.3 About the Code Implementation 24

5 Simulations, Results and Discussion 25

5.1 Code Verification 26

5.1.1 Invariance of the Motionless Solution 26
5.1.2 Verification with Critical Rayleigh Number 28
5.2 Convection in Two-Dimensional Porous Media 32
5.2.1 Without Faults 32
5.2.2 With Faults 35
5.3 Convection in Three-Dimensional Porous Media 38
5.3.1 Without Faults 39
5.3.2 With Faults 41
6 Conclusion 47
7 Bibliography 48

List of Symbols

The symbols used in this thesis, together with their respective units, are shown in the table below. Symbols written in bold are vectors, and tensors are denoted by bold capital letters.

Other than this, subscript f and s will be used for variables concerning fluid and solid respectively. Subscript 0 is used to specify a reference or starting value for a variable. Subscript or superscript h and l will denote properties or values connected with respectively higher and lower dimensional subdomains, and subscript k will be for variables concerning interfaces between these domains.

Some of the simulations serves a purpose of comparing results for different parameter values. These different parameter values will be denoted by a number subscript, in addition to the other subscripts this parameter may have from earlier.

Symbol	Physical parameter	Unit
$\boldsymbol{g}$	Gravitational acceleration vector	$\mathrm{m\ s^{-2}}$
$\boldsymbol{K}$	Permeability	$\mathrm{m^2}$
$\boldsymbol{\mathcal{K}}$	Hydraulic conductivity	$\mathrm{m\ s^{-1}}$
$\boldsymbol{u}$	Darcy velocity/Fluid flux	$\mathrm{m\ s^{-1}}$
$\boldsymbol{w}$	Advective heat flux	$\mathrm{J\ m^{-2}\ s^{-1}}$
$\boldsymbol{q}$	Conductive heat flux	$\mathrm{J\ m^{-2}\ s^{-1}}$
$\boldsymbol{\mathfrak{w}}$	Total heat flux	$\mathrm{J\ m^{-2}\ s^{-1}}$
$\boldsymbol{\Lambda}_e$	Effective thermal conductivity	$\mathrm{J\ s^{-1}\ m^{-1}\ K^{-1}}$
$\boldsymbol{f}$	General flux field	–
$\boldsymbol{n}$	Outward normal vector	–
ϕ	Porosity	–
l	Length	m
z	Height over datum	m
H	Vertical height of domain	m
h	Hydraulic head	m
a	Aperture	m
p	Pressure	Pa
T	Temperature	K
t	Time	s

Δt	Time-step	s
$\rho_{f,0}$	Reference fluid density	kg m^{-3}
ρ_f	Fluid density	kg m^{-3}
ρ_s	Rock density	kg m^{-3}
c_s	Rock specific heat	J kg^{-1} K^{-1}
c_f	Fluid specific heat	J kg^{-1} K^{-1}
Λ_s	Solid thermal conductivity	J $m^{-1}s^{-1}K^{-1}$
Λ_f	Fluid thermal conductivity	J $m^{-1}s^{-1}K^{-1}$
β_f	Thermal expansion coefficient	K^{-1}
μ	Dynamic viscosity	Pa s
$(\rho c)_e$	Effective volumetric heat capacity	J m^{-3} K^{-1}
Ra_c	Critical Rayleigh number	–
Ra	Rayleigh number	–
η	General conserved quantity	–
r	General source/sink term	–
h_h	Horizontal extension of domain	m
h_v	Vertical extension of domain	m
δ_T	Temperature deviation ratio	–
Δ	Increment	–
∇	Gradient	m^{-1}
$\nabla \cdot$	Divergence	m^{-1}

List of Figures

Figure 1.1: Convection cells in a 2D medium heated from below and cooled from above. The blue and red zones signify negative and positive temperature deviations, respectively, from a pure conductive solution (linear increase of temperature with depth). Arrows are added later for visualization purposes. 3

Figure 1.2: Up- and down-flow zones visualized in red and blue, respectively, for a three-dimensional porous media heated from below. 4

Figure 3.1: Schematic of Darcy's experiment. Figure is adapted from Nordbotten and Celia (2012, p. 18) 10

Figure 3.2: Example of two lower dimensional intersecting faults within a higher dimensional rock 14
Figure 3.3: Simple illustration of a higher and lower dimensional domain, Ωh and Ωl respectively, with their intersection line, Γk. Projection operators for mapping quantities to subdomains, subdomain boundary and the intersection are also present. Figure is adapted from Keilegavlen et al. (2021, p. 248) 15
Figure 4.1: Primal and dual grid refinement for the MPFA method. 21
Figure 5.1: a) Domain without the filter CellDatatoPointData applied. Cell edges are kept to clearly show the mesh..b) Domain after the filter CellDatatoPointData has been applied. 25
Figure 5.2: Schematic of the boundary conditions. 27
Figure 5.3: a) Initial Condition 1. b) Motionless solution. 28
Figure 5.4: a) Initial Condition 2. b) Motionless solution. 28
Figure 5.5: Verification case 1 with aspect ratio 0.5. a) Deviation ratio plotted against Rayleigh number where each dot represents an increment in permeability of $\Delta K = 0.6 \cdot 10 - 14\, m2$. Red dots signify the interval $[45.9,49.2]$ of which the critical Rayleigh number lies. b) ΔT result from Rayleigh number corresponding to $Ra = 49.2$. 30
Figure 5.6: Verification case 2 with aspect ratio 1. A) Deviation ratio plotted against Rayleigh number where each dot represents an increment in permeability of $\Delta K = 0.6 \cdot 10 - 14\, m2$. Red dots signify the interval $[28.7,32.1]$ of which the critical Rayleigh number lies. b) ΔT result from Rayleigh number corresponding to $Ra = 32.1$. 30
Figure 5.7: Verification case 3 with aspect ratio 4. A) Deviation ratio plotted against Rayleigh number where each dot represents a increment in permeability of $\Delta K = 0.6 \cdot 10 - 14\, m2$. Red dots signify the interval $[26.0, 29.3]$ of which the critical Rayleigh number lies. b) ΔT result from Rayleigh number corresponding to $Ra = 29.3$. 30
Figure 5.8: Simulation results of convection barely occurring due the Rayleigh number being just above the critical Rayleigh number. a) Shows the temperature profile of the system. b) Temperature deviation from the motionless solution. 33
Figure 5.9: Illustrations from a simulation with a high Rayleigh number, and therefore also noticeable convection. a) Temperature contours. b) Temperature deviation from the motionless solution. 34
Figure 5.10: Simulation 1/3 with a faulted two-dimensional domain. Corresponding parameter values are denoted by subscript 1 in the parameter table of this section. a) Regular temperature profile. b) Temperature deviation from motionless solution. 36

Figure 5.11: Simulation 2/3 with a faulted two-dimensional domain. Corresponding parameter values are denoted by subscript 2 in the parameter table of this section. a) Regular temperature profile. b) Temperature deviation from motionless solution..... 37
Figure 5.12: Simulation 3/3 with a faulted two-dimensional domain. Corresponding parameter values are denoted by subscript 3 in the parameter table of this section. a) Regular temperature profile. b) Temperature deviation from motionless solution..... 37
Figure 5.13: Schematic of three-dimensional domain..... 39
Figure 5.14: Simulation 1/2 in three-dimensional domain. The Rayleigh number is close to the critical value. Values for permeability and Rayleigh number will have subscript 1 in the table at the end of this section. a) Temperature profile, b) Temperature deviation contours from the motionless solution..... 40
Figure 5.15: Simulation 2/2 in three-dimensional domain. The Rayleigh number is a lot higher than the critical value. Values for permeability and Rayleigh number will have subscript 2 in the table at the end of this section. a) Temperature profile, b) Temperature deviation contours from the motionless solution. 40
Figure 5.16: Visualization of the fault location within the rock. The rock is here presented only by an outline and points, such that the faults are easier to see. 41
Figure 5.17: Temperature profiles in the rock is presented by fifteen temperature contours ranging from $\approx 273.15\ K$ to $\approx 473.15\ K$. Host rock is clipped such that we can see how the contours are linearly spaced at the corners furthest away from the fault intersection. a) Faults visible. b) Faults hidden. 42
Figure 5.18: Fifteen temperature contours ranging from $\approx 273.15\ K$ to $\approx 473.15\ K$ for simulation of three-dimensional domain with two intersecting faults. The domain is clipped at different locations to show the change in temperature contours with increased distance from the fault intersection. Clipped at: b) x = 900 m, c) x = 800 m, d) x = 700 m, e) x = 600 m. 43
Figure 5.19: Contours for temperature deviation in faulted three-dimensional domains. The domains are clipped in the middle, and the faults are hidden. Figures in the same column correspond to the same case. Columns 1 and 2 have parameters corresponding to subscript 1 and 2, respectively, in parameter table for this section. a) and c) are for the faults 10 times more permeable than host rock. b) and d) are for the faults 75 times more permeable than host rock. 44
Figure 5.20: Visualization of only the faults. Parameters for a) and b) correspond to those with subscript 1 and 2, respectively, in parameter table for this section. a) Temperature contours

within faults 10 times more permeable than host rock. b) Temperature contours within faults 75 times more permeable than host rock. 45

List of Tables

Table 5.1: Parameter values for the simulations. 26
Table 5.2: Horizontal domain extensions, time parameters, and non-linear tolerance for critical Rayleigh number verification. 29
Table 5.3: Grid refinement and non-linear tolerance for all two-dimensional simulations. 32
Table 5.4: Permeability and Rayleigh number for low-Rayleigh number simulation in two dimensions without faults. 34
Table 5.5: Permeability and Rayleigh number for high-Rayleigh number simulations in two-dimensions without faults. 35
Table 5.6: Grid refinement and time-parameters for the two-dimensional simulation. 35
Table 5.7: Parameters for motionless solution of faulted domain in two-dimensions. 36
Table 5.8: Fault permeabilities and overall CPU-time for the faulted, two-dimensional simulations. Simulation time and time-step is the same as for the motionless solution. 38
Table 5.9: Grid refinement and non-linear tolerance for three-dimensional simulations. 39
Table 5.10: Parameters for the three-dimensional simulations without faults. 41
Table 5.11: Parameters for the three-dimensional simulation with intersecting faults. 42
Table 5.12: Parameters for motionless, faulted, three-dimensional solution. 46
Table 5.13: Values for fault permeability and overall CPU-time for the faulted simulations showing temperature profiles for the temperature differences. 46

Outline

Chapter 1 presents the context of the research. We provide a short introduction to exploitation of venting minerals on the seafloor, which is the motivation behind studying the mathematical and numerical model in this thesis. Afterwards, we discuss convection in porous media and what determines the onset of convection. Lastly, contributions of this thesis are mentioned.

Chapter 2 presents the main properties of both the porous media and the fluid flowing through it. This allows the reader to better understand all parameters that are going to be introduced in Chapter 3, where the mathematical model used in this thesis is presented. We present the mathematical model by first defining a general conservation law for some quantity in a domain. Further on, the volume and energy conservation equations are presented from the general conservation law by introducing the respective constitutive laws for the flux terms. The second half of this chapter considers the model equations for the faults and fault intersections, and how the equations are coupled together by various coupling conditions.

Chapter 4 gives a general description of finite volume methods, multi-point flux approximation, the upwind scheme, and the implicit Euler time discretization. We present a short summary of what our code contribution involves, and how this work has its base in already existing code in PorePy. Verification of the code and all the simulation results are then presented in Chapter 5. We present two ways we have verified the code, and then proceed to show simulation results considering two- and three-dimensional domains with and without faults. Throughout this chapter we also provide discussion of the results presented. Finally, several discussion points and concluding remarks are presented in Chapter 6.

1 Introduction

This thesis presents a mathematical model for describing thermal single-phase flow in faulted porous media, numerical methods, and results from three-dimensional simulations of natural convection in faulted domains. The simulations consider parameters representative for the subseafloor, which is important to get a better understanding of the natural, buoyancy-driven convection processes going on there. In this chapter we will present our motivation for studying this, starting with a brief introduction to the theory of deep-sea ore deposits that occur close to oceanic spreading centers. Later on, the basics regarding natural convection is presented, and as a final note, the thesis contributions are outlined.

Deep-Sea Ore Deposits

In our everyday life, mineral resources as metals are crucial to keep up with production of the various modern technology products needed in our modern society (Graedel et al., 2015; Rötzer & Schmidt, 2018). Given the fact that the amount of mineral resources on Earth are limited, the constantly increasing demand of metals for production of for instance electric vehicles and cell phones, to only mention some, can ultimately lead to a metal deficit (Graedel et al., 2015).

This concern of a possible metal deficit leads us to have a look towards the deep sea, and more specifically what is happening in and just above the subseafloor. The ocean covering over two thirds of the Earth's surface leads to oceanic crust being the most bountiful crustal type on Earth, and the continuous movement of the tectonic plates throughout the seafloor can give life to hydrothermal deposit sites (German et al., 2016; Rona, 1984, 2003; Tao et al., 2020). These kinds of hydrothermal venting sites are important in the sense that the venting fluids may contain minerals, and mining these locations could be the next step in producing mineral resources to cope with a possible future metal deficit (Anderson, 2018; Rona, 2003).

As reported by Rona (2003) and Fouquet (2011), mineral-rich fluids are vented as follows: cold and dense sea water flows through the cracks in the oceanic crust, and as it descends it will get warmed up due to the temperature increase as one gets closer to the Earth's core. Then, the fluid ascends towards the surface again due to its now much lower density. On its way, the warm fluid interacts with the rock in its path, dissolving and transporting valuable minerals and metals. As the mineral rich fluid reaches the seafloor, the metals are finally discharged through vents called "black smokers" or seafloor massive sulfide deposits. These vents leads to clouds of metallic mineral particles precipitating on the seafloor (Coumou et al., 2008; Rona, 2003),

and such hydrothermal activity is what causes the creation of potential mining grounds for metals like Cu, Zn, Pb, Ag and Au (Anderson, 2018).

Convection in Porous Media

The main principle behind the creation of these potential mining sites, is the convective movement of fluid mentioned above. These areas of circulation will have locations where the fluid flows upwards, and other regions where the fluid flows downwards. One full cycle of fluid ascending, descending and then ascending again is called a convection cell, and multiple convection cells in a domain are altering between being clockwise and anti-clockwise (Zhao et al., 2008). A simplified illustration of the convection cells in a 2D-system heated from below is visualized in Figure 1.1. The up-flow zones are marked in red, and the down-flow zones in blue.

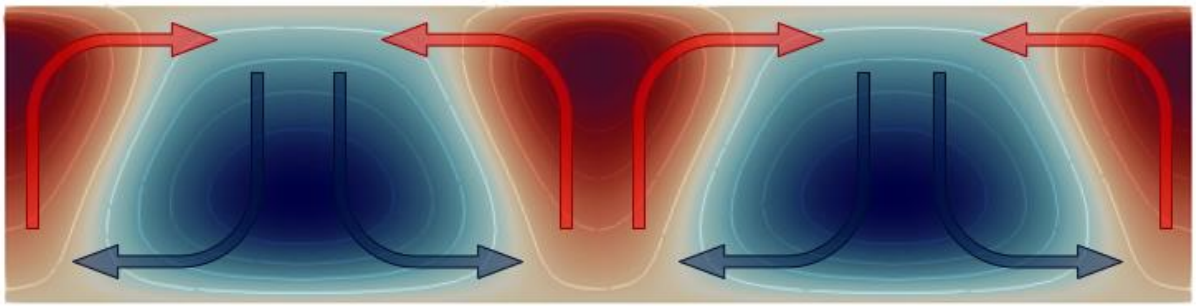

Figure 1.1: Convection cells in a 2D medium heated from below and cooled from above. The blue and red zones signify negative and positive temperature deviations, respectively, from a pure conductive solution (linear increase of temperature with depth). Arrows are added later for visualization purposes.

The clockwise/anti-clockwise way of thinking also holds in three dimensions. For each up-flow zone there are up to four neighboring down-flow zones, as opposed to in two dimensions, where there is only a maximum of two. This makes convection currents similar to those in Figure 1.1 appear in a star- or cross-like formation. An illustration of the up- and down-flow zones in three dimensions is presented in Figure 1.2.

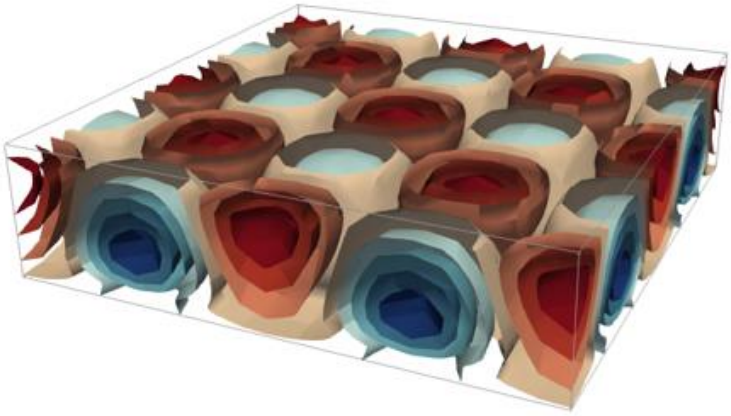

Figure 1.2: Up- and down-flow zones visualized in red and blue, respectively, for a three-dimensional porous media heated from below.

For convection to happen, either it is in two- or three dimensions, a certain criterion must be fulfilled. From a problem studied by Horton and Rogers (1945) and Lapwood (1948), later known as the Horton-Rogers-Lapwood problem, a critical value for the Rayleigh number was presented. The Rayleigh number is a convection parameter that, in a sense, is a measure of the competition between buoyant forces and viscous forces affecting a fluid. Higher Rayleigh number means that the buoyant forces are the driving forces, and spontaneous convection of the system may happen (Duwiquet et al., 2019; Kühn & Gessner, 2009; Patterson & Driesner, 2020). The expression for the Rayleigh number in a porous medium is given by Horton and Rogers (1945) and Lapwood (1948):

$$Ra = \frac{(\rho_{f,0} c_f)\rho_{f,0}\beta_f H g k \Delta T}{\Lambda_e \mu}$$

It must however be mentioned that the Rayleigh number required for spontaneous convection, also called the critical Rayleigh number, Ra_c, will vary depending on the problem formulation. Coming back to the Horton-Rogers-Lapwood problem, a homogeneous, infinite horizontal layer heated from below, with all impermeable boundaries was studied. The critical value they found for this kind of systems is $Ra_c = 4\pi^2 \approx 39.48$. We are, however, interested in studying domains with a permeable top at constant pressure. This is what resembles the conditions at the oceanic crusts (Tewari & Torrance, 1981), and therefore more relevant for the research in this thesis. Lapwood (1948) did a study on infinite rectangular domains with such boundary conditions, and in this case the critical value is $Ra_c = 27.1$. This shows how the problem formulation, in this case the boundary conditions, can have a great impact on the critical value.

As the particular problem we are considering in this thesis is finite, we cannot directly use exactly $Ra_c = 27.1$ for the critical value. Imposing spatial restrictions to the domain, i.e.,

making it finite, can change the critical Rayleigh number (Beck, 1972; Tewari & Torrance, 1981). In the case of finite domains with all impermeable boundaries, Beck (1972) found that Ra_c is bounded below by $4\pi^2$. A study performed by Tewari and Torrance (1981) found a similar result for the finite rectangular domain with a constant pressure permeable top: Ra_c is bounded below by the critical value for the "corresponding" infinite domain. By this we know that for the finite, constant pressure permeable top domains we consider, Ra_c is above or equal to 27.1.

Our focus when it comes to convection in this thesis is to study how convection is influenced by a faulted porous media. This is done both for Rayleigh numbers close to and significantly higher than Ra_c. The term fault will in this work be used about large locations within a domain where the permeability is higher than the one in the surrounding rock. Faults can be defined as large zones in the Earth crust where the surrounding rock is allowed to slide relative to each other. The faults are because of this relatively open, and therefore they have a higher permeability than the surrounding rock walls.

Focusing on fluid behavior in faulted systems can provide a deeper understanding of how real-life hydrothermal systems behave. More specifically, we can get a better insight into hydrothermal systems who contribute to creation of the mineral deposits mentioned above. These particular hydrothermal systems are located close to seafloor spreading centers where large faults are present (Rona, 1984), and this is our main motivation for studying how hydrothermal convection is impacted by the presence of faults.

Contributions

The main contribution of this thesis is the development of a python class for solving the coupled volume- and energy conservation equations to study convection in porous media. The code is implemented with PorePy (https://github.com/pmgbergen/porepy), an open-source Python framework.

The code can be used to simulate thermal single-phase flow in both (vertically) faulted and layered two- and three-dimensional porous media. This makes it relevant to use for studying real-life hydrothermal systems. Three-dimensions are necessary to observe properly how the hydrothermal convection mainly happens within the faults, and in comparison, only barely influences the temperature distribution in the host rock. It is therefore justified to do simulations in three dimensional domains.

2 Porous Media and Fluid Characteristics

This chapter presents basic properties of both the porous media and the fluid which will flow through it. First some properties of the porous media are presented, and then we move on to mention the fluid properties considered in this thesis. The last part of this subchapter briefly explains other properties that consider both the rock and the fluid. The theory presented in this chapter is based on Nordbotten and Celia (2012) and Huinink (2016).

2.1 Properties of Porous Media

Sandstone, granite, shale and basalt are only some examples of porous rocks, and what all these rock types have in common is their basic composition: they consist of one solid part, which is referred to as the matrix or the skeleton, and one part which is essentially just a void space, also called the pore space. These may work as a pathway for fluids to flow, and the ease of which this happens depends on the geometry of the pore space, and some fluid properties which will be brought up in detail later.

Due to the matrix' highly complex nature, simplifying our domain is necessary to solve problems within it. This is done by taking averages of the different variables throughout the matrix over a fitting length scale, and the length scale in question is called *Representative Elementary Volume* (REV). A REV should be large enough to contain a representative average of the domain, but also small enough to ensure it is possible to use continuous functions to approximate parameter variations between adjacent REVs.

One of the variables within the REV is porosity, and this is the ratio of the void space and the total volume of the REV:

$$\phi = \frac{void\ space\ within\ REV}{volume\ of\ REV}.$$

This leads us to another important property of the porous media, which is the permeability. Permeability describes how easy it is for a fluid to flow through the rock. Immediately one might think that a high porosity automatically means high permeability, but this is only the case if the pore space is connected. A fluid will not be able to pass through to an isolated pore and this is how the effective porosity, ϕ_E, is introduced. The most important part of how permeable a material is, is how the pore-space is connected. Therefore, will we from now on use the following definition of porosity:

$$\phi_E = \frac{connected\ void\ space\ within\ REV}{volume\ of\ REV}.$$

For simplicity we will in the rest of this thesis refer to this as only the porosity instead of effective porosity, and therefore also only use the symbol ϕ from now on. To provide some examples of porosity values, we will present the porosity of a few common rock types. Shale and fractured basalt has porosities somewhere between $0.00 - 0.10$ and $0.05 - 0.50$, respectively (Huinink, 2016). Another example is the porosity of a faulted, granite body at the Soultz-sous-Forêts geothermal site, which is reported to have a value between $0.05 - 0.15$ by Géraud et al. (2010).

2.2 Properties of the Fluid

The void space will either be filled with one or more fluids. In this thesis, one fluid fully saturating the porous space will be considered. The fluid forms a single-phase and its particles move through the matrix, resulting in a single-phase flow. Two or more fluids would be referred to as two-phase flow or multi-phase flow. In addition, the fluid we will examine do not have a constant density. The fluid density plays a significant role in this thesis since we are studying density driven convection of water. Generally, the density depends on both pressure and temperature, but we will in this thesis only consider density to be dependent on temperature. This justified due to the influence on density from pressure is a lot smaller than that of temperature, and the fluid density expression will be on the following form:

$$\rho_f = \rho_f(T).$$

As the temperature rises, the fluid expands, which results in a decrease in density. This can intuitively be understood by looking at the unit for density, which is [kg m^{-3}]. When the fluid expands, the volume it occupies is larger. Since the fluid volume appears in the denominator of the density unit, an increased volume will lead to a decrease in fluid density. The fluid density expression we have used will be presented in the next chapter.

Other than this, viscosity is also an important property of the fluid. Briefly explained, viscosity describes the fluid's resistance to flow, where a lower viscosity signifies that the fluid flows easier than if it has a higher viscosity. In the case of water, which is the fluid considered in this thesis, the viscosity has a value of around $\mu = 10^{-3}$ Pa s at a temperature of 20 °C. As the water is warmed up deep down in the subsurface, its viscosity will get lower and therefore it is less resistant to flow. For the sake of simplicity, we maintain the viscosity constant throughout this thesis.

2.3 Porous Media and Fluid Properties

Other important properties regarding fluid and heat transfer in porous media, is hydraulic conductivity, thermal conductivity, specific heat, and volumetric heat capacity. Hydraulic conductivity is proportional to the rock permeability and is a way to measure how easy a fluid may flow through a porous medium. The hydraulic conductivity also depends on fluid density and viscosity, which means that it takes into consideration how "flowable" the fluid is. The next chapter will provide more details about the hydraulic conductivity.

Thermal conductivity is a measure of how easily heat is transferred through a material, where a higher value means better heat transfer abilities. For the rock and fluid considered in this thesis, the thermal conductivity has values of $3.35\ [\mathrm{J\,s^{-1}m^{-1}K^{-1}}]$ and $0.6\ [\mathrm{J\,s^{-1}m^{-1}K^{-1}}]$, respectively. In other words, the rock has a better heat transfer ability than the fluid.

The quantity specific heat appears in our model equations through the conservation law for the energy, which will presented in the next chapter. A material's specific heat is the amount of heat required to raise one gram of the material by one degree Kelvin. For the materials we have considered, the specific heat of the fluid is over four times larger than that of the rock, meaning that it requires more heat to raise the fluid temperature than the rock temperature.

The volumetric heat capacity is a quantity closely related to the specific heat, since it is the specific heat multiplied by the density of the material. Volumetric heat capacity is a measure of the heat needed to cause a temperature increase of one degree Kelvin of one unit volume of the body. The definitions of specific heat and volumetric heat capacity can be found in a suitable textbook, for instance one about thermodynamics, or in an online dictionary.

3 Governing Equations

This chapter presents the governing equations for the mathematical model solved in this thesis. First a general model for volume and heat transfer in porous media is presented, and then this is expanded to also consider faults within the porous media. The theory in the sections up until the part concerning heat is based on Nordbotten and Celia (2012). References for the proceeding parts will be specified throughout the text.

3.1 Flow and Heat Transfer in Porous Media

A very fundamental principle of conservation of a quantity is considered when modelling flow in porous media. Conservation equations can be presented in the following way: the change of a quantity within a domain is equal to the sum of what flows through the domain boundaries, and the internal sources or sinks within the domain. This principle can be shown through the following mathematical formula, which is a general form of such a conservation equation:

$$\int_{\Omega} \frac{\partial \eta}{\partial t} dV = -\oint_{\partial\Omega} \boldsymbol{f} \cdot \boldsymbol{n}\, dA + \int_{\Omega} r dV. \tag{3.1}$$

Here, the left-hand side is the change of the conserved quantity, η, within the domain, Ω. The first term on the right-hand side represents what flows into the domain through its boundaries, where $\boldsymbol{f}$ is the flux field, and $\boldsymbol{n}$ is the outer unit normal vector of the domain. Contributions from internal sources or sinks, r, within the domain are represented by the last term.

Equation (3.1) can be rewritten by applying the divergence theorem to the surface integral:

$$\int_{\partial\Omega} \boldsymbol{f} \cdot \boldsymbol{n}\, dA = \int_{\Omega} \nabla \cdot \boldsymbol{f}\, dV, \tag{3.2}$$

which leads to the following expression for our conservation equation:

$$\int_{\Omega} \frac{\partial \eta}{\partial t} dV + \int_{\Omega} \nabla \cdot \boldsymbol{f}\, dV = \int_{\Omega} r\, dV. \tag{3.3}$$

This holds for any arbitrary, closed volume, Ω. After applying the localization theorem, the integral conservation equation is converted to a partial differential equation for the conserved quantity, η (Gurtin, 1981):

$$\frac{\partial \eta}{\partial t} + \nabla \cdot \boldsymbol{f} = r. \tag{3.4}$$

Equation (3.4) is what will form the baseline for defining the conservation equations in this chapter. In this thesis the conservation equations are of volume and energy, and each of them

will be presented by defining the constitutive laws for the respective equations. Also, no internal source or sink terms is considered for the equations in this thesis, and therefore we will define them to be zero.

3.1.1 Darcy's Law and Volume Conservation

When dealing with mass conservation of a flowing fluid, the conserved quantity, η, the flux field, $\boldsymbol{f}$, and the source/sink, r, are in the case of this thesis defined as:

$$\eta = \rho_f \phi, \qquad \boldsymbol{f} = \rho_f \boldsymbol{u}, \qquad r = 0. \tag{3.5}$$

Which leads to the following expression for the mass conservation equation:

$$\frac{\partial \rho_f \phi}{\partial t} + \nabla \cdot (\rho_f \boldsymbol{u}) = 0. \tag{3.6}$$

Here ϕ is the porosity of the medium and $\boldsymbol{u}$ is the fluid flux. Further down in this section we will elaborate upon the fluid density and introduce a constitutive law for the fluid flux in (3.6).

To present this we will start by introducing how the engineer Henry Darcy in 1856 performed an experiment, where the results led to what is known as Darcy's law today. The experiment was about investigating the amount of water flowing through a column of sand, and the result of this experiment gives us the expression for the fluid flux in Equation (3.6). Figure 3.1 shows an illustration of the experiment.

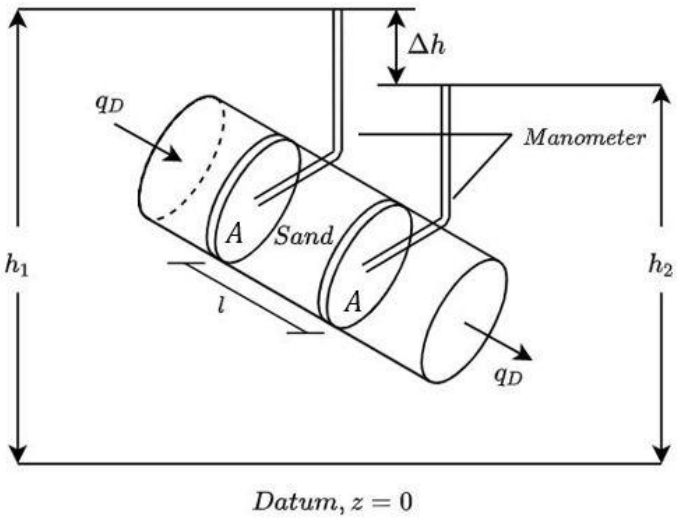

Figure 3.1: Schematic of Darcy's experiment. Figure is adapted from Nordbotten and Celia (2012, p. 18)

The experiment presented for Darcy three observations regarding the flow of water through a sand filter. Two of which is that volumetric flow rate, q_D, is proportional to both the cross-sectional area, A, and the difference $(h_2 - h_1)$. His third observation was the volumetric flow

rate's inversely proportional relation to the length between the two measuring points, l. These three observations lead to Equation (3.7):

$$q_D = \mathcal{K} \frac{A(h_2 - h_1)}{l}. \tag{3.7}$$

Here, $\mathcal{K}$ is a positive proportionality coefficient, which will later be referred to as hydraulic conductivity. Dividing Equation (3.7) by the cross-sectional area, A, gives an expression for the volumetric flow rate per area, i.e., the flux, u.

$$u \equiv \frac{q_D}{A} = \mathcal{K} \frac{h_2 - h_1}{l}. \tag{3.8}$$

Taking the limit for $l \to 0$ of Equation (3.8) leads us to the differential form of Darcy's law:

$$\boldsymbol{u} = -\boldsymbol{\mathcal{K}} \nabla h. \tag{3.9}$$

Darcy's law is here expressed as a function of hydraulic head, h, which is a measure of the fluid pressure at the measuring point. The hydraulic head is dependent on fluid pressure, p, fluid density, ρ_f, gravitational acceleration, g, and the elevation above the datum, z, and takes the following form:

$$h = \frac{p}{\rho_f g} + z. \tag{3.10}$$

The *hydraulic conductivity*, $\boldsymbol{\mathcal{K}}$, in Equation (3.9), is an important property of flow in porous media. Hydraulic conductivity describes how easy a fluid can flow through a material in certain directions and locations and is defined as shown below:

$$\boldsymbol{\mathcal{K}} = \frac{\boldsymbol{K} \rho_f g}{\mu}. \tag{3.11}$$

Here $\boldsymbol{K}$ is the material permeability, ρ_f is the fluid density, and μ is the fluid viscosity. The permeability, and therefore also the hydraulic conductivity, can be either scalars or tensors. For an anisotropic and/or heterogeneous porous media, they will be tensors. This is due to the ease fluid flow being dependent on the flow direction and/or position. If the media is homogeneous and isotropic, fluid flows as easy in one direction and location as any other, and they will therefore only be scalar quantities.

Using the defined expressions for the hydraulic head and the hydraulic conductivity, we can rewrite Darcy's law to its pressure formulation:

$$\boldsymbol{u} = -\frac{\boldsymbol{K}}{\mu}\left(\nabla p - \rho_f \boldsymbol{g}\right). \tag{3.12}$$

This is the expression we have used for the fluid flux, and it is the flux expression that will appear in the conservation equation for the fluid flow.

Moving on to the final adjustments of the mass conservation equation, we need to further specify how the fluid density is varying. Density is in our case only assumed dependent on temperature and is assumed to follow the expression below. This holds due to the assumption that the flow considered is only slightly expandable.

$$\rho_f(T) = \rho_{f,0} \exp\left[-\beta_f (T - T_0)\right]. \tag{3.13}$$

Which can be linearized to:

$$\rho_f(T) \approx \rho_{f,0}\left[1 - \beta_f (T - T_0)\right]. \tag{3.14}$$

Here $\rho_{f,0}$ is the reference fluid density and β_f is the thermal expansion coefficient of the fluid, where the latter is defined by the following expression:

$$\beta_f = \frac{1}{\rho_f}\frac{\partial \rho_f}{\partial T}.$$

Linearizing the density like this and then dividing the entire expression for the mass conservation equation by $\rho_{f,0}$, the equation instead becomes a volume conservation equation. We then arrive at the following conservation equation for the volume:

$$-\phi \beta_f \frac{\partial T}{\partial t} + \nabla \cdot \boldsymbol{u} = 0, \tag{3.15}$$

where $\boldsymbol{u}$ is determined by Equation (3.12).

Note that one assumption regarding the second term in Equation (3.15) has been made. This term originally considers the divergence of both fluid density and Darcy velocity. Using the product rule on this term, we notice the term $\boldsymbol{u} \cdot \nabla \rho_f$ appears. This is assumed to be so small that it can be neglected (Nordbotten & Celia, 2012, p. 34).

3.1.2 Heat Flux and Energy Conservation Equation

In the same manner as with the volume conservation equation, we present the conservation equation for the energy in our system. This is done by following the presentation by Stefansson, Berre, et al. (2021), with the exception that we take the source term to be zero. Therefore, we impose the following to Equation (3.4):

$$\eta = (\rho c)_e T, \qquad \boldsymbol{f} = \mathfrak{w}, \qquad r = 0, \tag{3.16}$$

which immediately gives the following expression for the energy conservation equation:

$$\frac{\partial (\rho c)_e T}{\partial t} + \nabla \cdot \mathfrak{w} = 0. \tag{3.17}$$

The flux is now $\mathfrak{w}$, being the total heat flux. The conserved quantity of our system has become the product of the temperature, T, and the effective volumetric heat capacity of the porous medium, $(\rho c)_e$. Due to an assumption of local thermal equilibrium, only a single temperature will be unknown, and therefore the effective coefficients come into the model. All these coefficients are denoted by subscript "e", which is computed by Equation (3.18) following the presentation by Stefansson et al. (2021):

$$(\cdot)_e = \phi(\cdot)_f + (1-\phi)(\cdot)_s. \tag{3.18}$$

The constitutive law for the flux in the energy conservation equation is the total heat flux, which is the sum of the advective and the diffusive flux. The expression for the total heat flux is:

$$\mathfrak{w} = \rho_f(T) c_f T\, \boldsymbol{u} - \boldsymbol{\Lambda}_e \nabla T. \tag{3.19}$$

Here c_f is the specific heat of the fluid and $\boldsymbol{\Lambda}_e$ is the effective thermal conductivity. In order to find the expression we want for the energy conservation equation, we use the chain rule of differentiation on the first term of Equation (3.17), and then we impose the linearization for the fluid density as we presented in Equation (3.14):

$$\frac{\partial (\rho c)_e T}{\partial t} = -\rho_{f,0} c_f \phi T \beta_f \frac{\partial T}{\partial t} + (\rho c)_e \frac{\partial T}{\partial t}.$$

This gives us the following expression for the energy conservation equation in porous media:

$$-\rho_{f,0} c_f \phi T \beta_f \frac{\partial T}{\partial t} + (\rho c)_e \frac{\partial T}{\partial t} + \nabla \cdot \mathfrak{w} = 0. \tag{3.20}$$

The Equations (3.15) and (3.20), together with their respective constitutive laws, some appropriate boundary conditions and initial conditions will form a model for thermal single-phase flow in porous media. We will come back to general expressions for this in the next subchapter which will present equations for thermal single-phase flow in faulted porous media.

3.2 Flow and Heat Transfer in Faulted Porous Media

The principles for the equations governing flow in faulted porous media are pretty much the same as the ones presented above, but with some modifications to consider the different geometry of the faults compared to that of the porous matrix. We will not go through the entire derivation of these equations, and we refer to Martin et al. (2005) and Berre et al. (2021) for a more detailed presentation. This subchapter will first present the geometric representation of the faulted porous media, then some projection notations gathered from Keilegavlen et al. (2021) will be explained. After this the equations themselves will be presented.

3.2.1 Geometric Representation of Faulted Porous Media

The faulted porous matrix is modelled by a mixed-dimensional discrete fracture matrix (DFM) model implemented in the open-source Python software PorePy (Keilegavlen et al., 2021). This is a way to model a faulted domain where the matrix, faults, and fault intersections are represented explicitly as individual subdomains of different dimensions. In a three-dimensional domain, for instance, the faults are represented by objects of dimension two. Reducing the dimensions like this is justified due to the faults being so thin compared to the rest of their extensions (Berre et al., 2021). Intersections between these faults are one-dimensional lines, and further intersections between these are zero-dimensional points (Keilegavlen et al., 2021). An example of two-dimensional, intersecting faults within a three-dimensional rock is shown in Figure 3.2. This is one of the domains we will present simulation results from in Chapter 5.

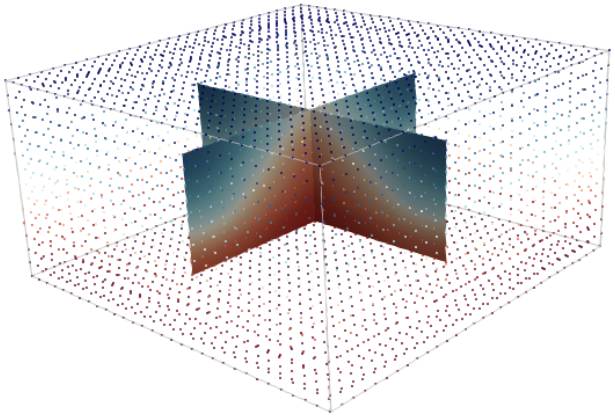

Figure 3.2: Example of two lower dimensional intersecting faults within a higher dimensional rock

All equations, variables and parameters present in the mathematical model is defined for each subdomain in the mixed-dimensional domain. Further on these are coupled together by treating the interface between them as some sort of "pit-stop" for projections of variables between the subdomains. The flow and transport equations in the lower dimensional subdomains are obtained by integrating the matrix equations in the normal direction of the fault. Faults are very thin, and therefore it is justified to reduce the dimensions of the matrix equations to equations of the faults by integrating them like this. This is called reduction of dimensionality (Berre et al., 2021).

In Figure 3.3 there is a simple illustration of one higher and one lower dimensional subdomain, Ω_h and Ω_l, that coincides geometrically, together with the intersection between them, Γ_k.

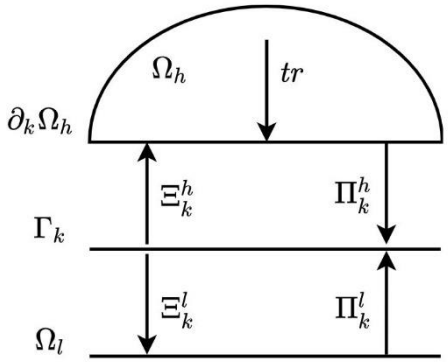

Figure 3.3: Simple illustration of a higher and lower dimensional domain, Ω_h and Ω_l respectively, with their intersection line, Γ_k. Projection operators for mapping quantities to subdomains, subdomain boundary and the intersection are also present. Figure is adapted from Keilegavlen et al. (2021, p. 248)

The trace operator, tr, shown in Figure 3.3 maps the variable from the higher dimensional domain to its boundary, $\partial_k\Omega_h$. The other operators shown in this figure can be split into two parts: those who project variables from an interface, Ξ, and those projecting to an interface, Π. The subscript of these projection operators denotes the interface they concern, while the superscript represents the subdomain. For example, a projection from the lower dimensional subdomain to the interface would have the operator notation Π_k^l. It is through these projections the coupling variables between the different subdomains are connected.

3.2.2 Conservation Equations for Flow in a Faulted Domain

Recall the fluid and total heat flux being denoted by $\boldsymbol{u}$ and $\mathbf{w}$, and recall the mixed dimensional coupling notation presented in the previous section. In this section we will present the lower-dimensional volume- and energy balance equations, which is given as presented by Berre et al. (2021), Stefansson, Berre, et al. (2021) and Stefansson, Keilegavlen, et al. (2021). For distinguishing between the divergence/gradient operator in the differently dimensioned

subdomains, subscript 1D and 2D will be used for dimension 1 and 2, respectively. These gradients and divergences will be parallel to the domain they are in. No subscript on the del-operator indicates that it belongs in three dimensions.

After performing a dimension reduction on the conservation equations for volume and energy, Equation (3.15) and Equation (3.20), respectively, we arrive at the following expressions for the conservation equations in the faults:

$$-a\beta_f \frac{\partial T}{\partial t} + a\,\nabla_{2\mathrm{D}} \cdot \boldsymbol{u} = \sum_{k \in S} \Xi_k^l(u_k), \tag{3.21}$$

$$-a\rho_{f,0} c_f T \beta_f \frac{\partial T}{\partial t} + a(\rho c)_e \frac{\partial T}{\partial t} + a\,\nabla_{2\mathrm{D}} \cdot \boldsymbol{\mathfrak{w}} = \sum_{k \in S} \Xi_k^l(w_k + q_k). \tag{3.22}$$

Doing another dimension reduction, the expression for the conservation equations in the fault intersection follow the expressions below:

$$-a^2\,\beta_f \frac{\partial T}{\partial t} + a^2\,\nabla_{1\mathrm{D}} \cdot \boldsymbol{u} = a \sum_{k \in S} \Xi_k^l(u_k), \tag{3.23}$$

$$-a^2\rho_{f,0} c_f T \beta_f \frac{\partial T}{\partial t} + a^2(\rho c)_e \frac{\partial T}{\partial t} + a^2\,\nabla_{1\mathrm{D}} \cdot \boldsymbol{\mathfrak{w}} = a \sum_{k \in S} \Xi_k^l(w_k + q_k). \tag{3.24}$$

The aperture, a, accounts for the reduction of dimensions, and S is the set of interfaces between the lower- and higher-dimensional subdomains. u_k, q_k and w_k are, respectively, fluid flux, conductive heat flux and advective heat flux for the interfaces. The expressions for these will be presented in the next section since they are coupling conditions for our model equations.

3.2.3 Coupling Conditions

To complete the model, we need to specify the coupling conditions between the conservation equations for higher- and lower dimensional subdomains. These are given as presented by Stefansson, Berre, et al. (2021) and Stefansson, Keilegavlen, et al. (2021).

The three interface fluxes mentioned in the previous section are one part of the coupling conditions between the equations concerning different subdomains. Internal boundary conditions are the other part that serves a coupling between the different domains, and will be presented shortly after the expressions for the interface fluxes shown below:

$$\begin{aligned} u_k &= -\frac{K_k}{\mu}\left(\frac{2}{a}\left(\Pi_k^l p_l - \Pi_k^h\,\mathrm{tr}(p_h)\right)\right), \\ q_k &= -\Lambda_k \frac{2}{a}\left(\Pi_k^l T_l - \Pi_k^h\,\mathrm{tr}(T_h)\right), \end{aligned} \tag{3.25}$$

$$w_k = \begin{cases} \rho_{f,h} c_f \Pi_k^h T_h \, u_k, & \text{if } u_k > 0 \\ \rho_{f,l} c_f \Pi_k^l T_l \, u_k, & \text{if } u_k \leq 0 \end{cases}.$$

K_k and Λ_k are the normal permeability and heat conductivity respectively. Note that the gravitational term in the fluid interface flux is removed. This holds due to the faults considered in this thesis is only going to be vertical.

Also, these interface fluxes must be used with some "caution" in the conservation equations. The expressions for interface fluxes between matrix-faults and faults-fault intersections are the same up to one factor, being the aperture. This weighting is taken care of in the respective conservation equations, and therefore the interface flux expressions are "the same" for both different interface types. Using these it is important to beware of subscripts l and h will denote different subdomains for the two different intersection types.

Subscript	l	h
1D interface	Fault intersection	Fault
2D interface	Fault	Matrix

The internal boundary conditions for the higher dimensional subdomains will complete the coupling, and expressions for these, on the boundaries $\partial_k \Omega_h$, are the following:

$$\boldsymbol{u}_h \cdot \boldsymbol{n}_h = \Xi_k^h \, u_k, \qquad \boldsymbol{w}_h \cdot \boldsymbol{n}_h = \Xi_k^h \, w_k, \qquad \boldsymbol{q}_h \cdot \boldsymbol{n}_h = \Xi_k^h \, q_k.$$

3.3 Model Equations

This subsection summarizes of all the equations we have presented, such that all of them are collected and easily found in the same place. These equations, together with the governing equation for the fluid density, and some initial and boundary conditions, form the mathematical model considered in this thesis.

Volume conservation for the porous matrix, faults, and fault intersections, respectively:

$$-\phi \beta_f \frac{\partial T}{\partial t} + \nabla \cdot \boldsymbol{u} = 0,$$

$$-a \beta_f \frac{\partial T}{\partial t} + a \, \nabla_{2\mathrm{D}} \cdot \boldsymbol{u} = \sum_{k \in S} \Xi_k^l(u_k),$$

$$-a^2 \, \beta_f \frac{\partial T}{\partial t} + a^2 \, \nabla_{1\mathrm{D}} \cdot \boldsymbol{u} = a \sum_{k \in S} \Xi_k^l(u_k).$$

Darcy velocity:

$$\boldsymbol{u} = -\frac{\boldsymbol{K}}{\mu}\left(\nabla p - \rho_f \boldsymbol{g}\right).$$

Note that the gradient is taken in the relevant domain. For instance, in two dimensional faults the gradient will consider only the directions parallel to the faults.

Energy conservation for the porous matrix, faults, and fault intersections, respectively:

$$-\rho_{f,0} c_f \phi T \beta_f \frac{\partial T}{\partial t} + (\rho c)_e \frac{\partial T}{\partial t} + \nabla \cdot \boldsymbol{\mathfrak{w}} = 0,$$

$$-a\rho_{f,0} c_f T \beta_f \frac{\partial T}{\partial t} + a(\rho c)_e \frac{\partial T}{\partial t} + a\, \nabla_{2\mathrm{D}} \cdot \boldsymbol{\mathfrak{w}} = \sum_{k \in S} \Xi_k^l (w_k + q_k),$$

$$-a^2 \rho_{f,0} c_f T \beta_f \frac{\partial T}{\partial t} + a^2 (\rho c)_e \frac{\partial T}{\partial t} + a^2\, \nabla_{1\mathrm{D}} \cdot \boldsymbol{\mathfrak{w}} = a \sum_{k \in S} \Xi_k^l (w_k + q_k).$$

Total heat flux:

$$\boldsymbol{\mathfrak{w}} = \rho_f(T) c_f T\, \boldsymbol{u} - \boldsymbol{\Lambda}_e\, \nabla T.$$

Also here the gradient is corresponding to the dimension of the subdomain in question.

Interface fluid flux, conductive heat flux and advective heat flux, respectively:

$$u_k = -\frac{K_k}{\mu}\left(\frac{2}{a}\left(\Pi_k^l p_l - \Pi_k^h \operatorname{tr}(p_h)\right)\right),$$

$$q_k = -\Lambda_k \frac{2}{a}\left(\Pi_k^l T_l - \Pi_k^h \operatorname{tr}(T_h)\right),$$

$$w_k = \begin{cases} \rho_{f,h} c_f \Pi_k^h T_h\, u_k, & \text{if } u_k > 0 \\ \rho_{f,l} c_f \Pi_k^l T_l\, u_k, & \text{if } u_k \leq 0 \end{cases}.$$

Linearized fluid density:

$$\rho_f(T) \approx \rho_{f,0}\left[1 - \beta_f (T - T_0)\right].$$

Internal boundary conditions for a higher dimensional subdomain:

$$\boldsymbol{u}_h \cdot \boldsymbol{n}_h = \Xi_k^h u_k, \qquad \boldsymbol{w}_h \cdot \boldsymbol{n}_h = \Xi_k^h w_k, \qquad \boldsymbol{q}_h \cdot \boldsymbol{n}_h = \Xi_k^h q_k.$$

External boundary conditions for the pressure and temperature are the following:

$$p|_{\partial\Omega_\mathrm{h}} = p_D, \qquad \boldsymbol{u}\cdot\boldsymbol{n}|_{\partial\Omega_\mathrm{h}} = u_N,$$

$$T|_{\partial\Omega_\mathrm{h}} = T_D, \qquad \boldsymbol{w}\cdot\boldsymbol{n}|_{\partial\Omega_h} = w_N.$$

Where subscript D and N denotes Dirichlet and Neumann conditions, respectively. Only constant values for the boundary conditions are used in this project.

Lastly, we present initial conditions for the pressure and temperature:

$$p(\boldsymbol{x}, t=0) = p_0(\boldsymbol{x}), \qquad T(\boldsymbol{x}, t=0) = T_0(\boldsymbol{x}),$$

where $\boldsymbol{x}$ is the spatial position within the domain.

4 Numerical methods

To solve the partial differential equations presented in this thesis, we have used finite volume multi-point flux approximation (FV-MPFA), the upwind scheme and implicit Euler for discretization. The first subchapter will present the FV-MPFA method, and is gathered from Nordbotten and Keilegavlen (2021) and the documentation of PorePy (Keilegavlen et al., 2021). The proceeding section presents the upwind scheme used for approximating the advective heat flux, and in the next subchapter we present the time discretization. Finally, we give a brief presentation of the work with our code for solving the governing equations in this thesis.

The numerical methods used for the code have been used as they are implemented in PorePy. Implementation of the numerical methods has therefore not been a focus during the work of this project, and only a brief explanation of the methods will be presented here.

4.1 Finite Volume Methods and Flux Approximation

Now we will present the basics of finite volume methods, and how they are applied to a conservation law. For presenting the finite volume methods, we are considering the conservation equation presented in Chapter 3:

$$\int_{\omega_i} \frac{\partial \eta}{\partial t}\, dV + \oint_{\partial \omega_i} \boldsymbol{f} \cdot \boldsymbol{n}\, dA = \int_{\omega_i} r\, dV, \tag{4.1}$$

where ω_i is one of several non-overlapping subdomains of Ω ($\omega_i \subset \Omega$), also referred to as control volumes or cells. In this subdomain we are in general considering the conserved quantity, η, and how this is affected by $\boldsymbol{f}$, $\boldsymbol{n}$ and r which are the flux field, the outward normal vector of ω_i and any internal sources or sink terms within the domain, respectively. However, we are for now only interested in the spatial discretization, so the temporal term will be temporarily discarded and then revisited in Subchapter 4.2.

The general idea of a finite volume method is to compute the flux of a substance through the surface, here $\partial\omega_i$, of the control volume. We define faces within the domain as intersections between two neighboring control volumes, and the collection of all faces of a cell ω_i is denoted $\mathcal{F}_i$. This leads to the following rewriting of the non-temporal terms of Equation (4.1):

$$\sum_{\sigma \in \mathcal{F}_i} \int_{\sigma} \boldsymbol{f} \cdot \boldsymbol{n}_{\sigma,i}\, dS = \int_{\omega_i} r\, dV. \tag{4.2}$$

Recognizing the left-hand side as the sum of fluxes over the cell faces σ for a cell ω_i, leads to the following expression, which is the form of which any finite volume method may be written:

$$\sum_{\sigma \in \mathcal{F}_i} q_{\sigma,i} = \int_{\omega_i} r \, dV, \tag{4.3}$$

where $q_{\sigma,i}$ is the integrated fluxes over cell face σ of ω_i. This holds for all cells ω_i in the partition of Ω. The method has local flux balance if the following holds for any $\sigma = \partial\omega_{i_1} \cap \partial\omega_{i_2}$:

$$q_{\sigma,i_1} = -q_{\sigma,i_2}.$$

4.1.1 Multi-Point Flux Approximation

Flux can be approximated in several different ways, and one of which is the multi-point flux approximation (MPFA). MPFA is based on the simpler two-point flux approximation, which determines the flux over a face by considering the potentials in the two cells neighboring the face. This method of approximating flux is however too simple, and the MPFA methods were developed. The numerical flux field, q_σ, we presented in the previous section is to be determined with the use of MPFA, and more specifically, it is the O-method that is implemented in PorePy and therefore used in this work. A brief introduction to this method is provided below.

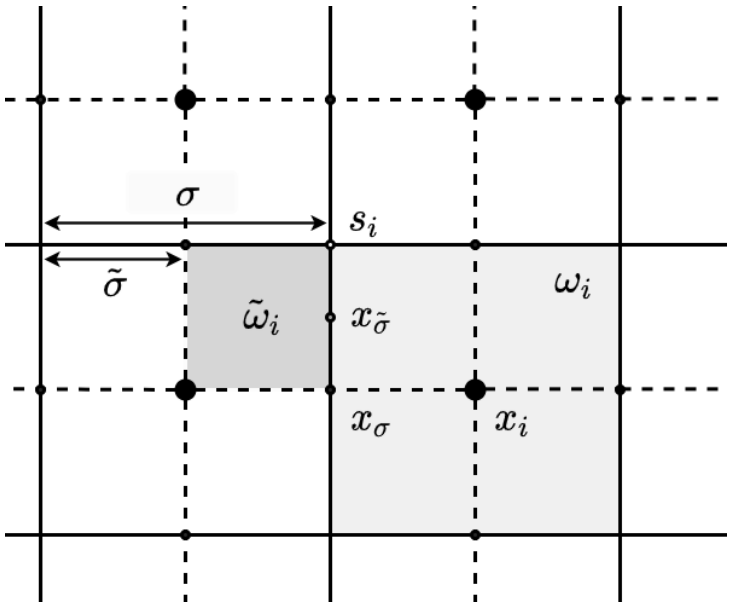

Figure 4.1: Primal and dual grid refinement for the MPFA method.

To perform a flux approximation, we start off with the solid, black line partition of our domain shown in the Figure 4.1 where the control volumes are denoted ω. This partition will be called the primal grid, and an example of a control volume of this grid is highlighted in a light shade of grey in the figure. This domain will however be "modified" by adding an extra grid structure, such that the MPFA method can be used. This grid will be called the dual grid and is shown in dashed lines, and s_i is the center of a cell in this grid. The construction of the dual grid is based on lines between the cell centers, x_i, of the control volumes, and the centers, x_σ, of the faces corresponding to the control volume.

The intersections between the primal and dual grid gives us the more refined sub-grid, whose cells will be denoted $\tilde{\omega}$ and called sub-cells. These are quadrilaterals with two dashed and two solid black faces, and one example of such a sub-cell is highlighted in a darker shade of grey. Further on, the faces of the sub-cell, the sub-faces, will be called $\tilde{\sigma}$, and the face centers are called $x_{\tilde{\sigma}}$.

The flux Is in this scheme not approximated over the cell faces, σ, but rather over each of the sub-faces, $\tilde{\sigma}$. To do this, the potential field needs to be discretized, and this is done such that the potential is described by a linear function on each of the sub-cells. A continuity of the potential is enforced at the cell centers. The flux field is so derived from the potential field, and when the potential is linear on each sub-cell, the flux field will be constant. When it comes to continuity in the flux, local flux balance is enforced over the sub-faces, and the following holds for the integrated fluxes:

$$\int_{\tilde{\sigma}} \boldsymbol{f} \cdot \boldsymbol{n}_{\tilde{\sigma},i_1} dS = -\int_{\tilde{\sigma}} \boldsymbol{f} \cdot \boldsymbol{n}_{\tilde{\sigma},i_2} dS \equiv q_{\tilde{\sigma}}.$$

In the end, the face flux, q_σ, is constructed by summing up all the sub-face fluxes, $q_{\tilde{\sigma}}$ corresponding to a cell face.

4.1.2 Upwind Scheme for the Advection Term

For the advective part of the total heat flux, $\boldsymbol{w}$, in the heat equation (shown in Equation (3.19)), we have used an upwind scheme for discretizing. Recalling the heat flux expression appearing in the heat balance and identifying the advective flux as the first term of this, leads us to the following equation for the advective flux:

$$\boldsymbol{w} = \rho_f(T)\, c_f T\, \boldsymbol{u}.$$

The upwind scheme takes into account where the fluid is coming from when we are considering flow through a subdomain's boundaries. The advected quantities in this case are the fluid density, fluid specific heat capacity and the temperature. In order to know for what values of p and T these are going to be evaluated, we measure the sign of the flux, $\boldsymbol{u}$, through the subdomain boundaries. Finding out in which direction the fluid is flowing for each face gives us information regarding which values to use.

This is expressed the following way for fluid flowing from a cell i to a neighboring cell j.

$$\left(\rho_f(T)c_f T\,\boldsymbol{u}\right)_{i,j} = \begin{cases} \rho_f(T_i)c_f T_i\,\boldsymbol{u}_{i,j}, & \text{if} \quad \boldsymbol{u}_{i,j} > 0 \\ \rho_f(T_j)c_f T_j\,\boldsymbol{u}_{i,j}, & \text{if} \quad \boldsymbol{u}_{i,j} \leq 0 \end{cases}. \tag{4.4}$$

The above expression follows the presentation by Stefansson, Berre, et al. (2021) but we refer to Courant et al. (1952) for details about this scheme.

4.2 Discretization in Time

Discretizing equations in time can be done in several ways, and the main thing to choose is whether the discretization is to be explicit or implicit. To present the main idea behind discretization in time, we are just going to consider the following simple differential equation:

$$\frac{d\eta}{dt} = F(\eta), \tag{4.5}$$

where η is the unknown quantity, and it is to be determined in terms of F. To solve this numerically, we need to approximate the derivative on the left-hand side. Doing this using a simple finite difference scheme gives us:

$$\frac{d\eta}{dt} \approx \frac{\eta^{n+1} - \eta^n}{\Delta t}.$$

This new expression is now using two different values of the quantity η to make an approximation for the derivative. From here there are two ways to approximate to the next value of η. We could either find η^{n+1} evaluating F at the current time, or we evaluate it at the next time step. The first one is called explicit Euler time-stepping and converts our simple differential equation into this:

$$\eta^{n+1} = \eta^n + \Delta t\, F(\eta^n).$$

For this to work, our time step would need to be sufficiently small. Fully explicit schemes have a time-step constraint which is quadratic in the length scale of the spatial discretization of the

problem (Nordbotten, 2015), which makes the fully explicit schemes are rather picky in terms of the step-size.

We have employed the implicit Euler time-stepping method in this thesis. It differs from the explicit time-stepping only in the fact that F is evaluated at η^{n+1}:

$$\eta^{n+1} = \eta^n + \Delta t\, F(\eta^{n+1}).$$

The time-step can either be fixed, or it can vary throughout the solution process of the problem. In the simulations we have performed, this value is kept fixed.

4.3 About the Code Implementation

Prior to the start of this work, a model class for solving incompressible flow in porous media was already present in PorePy, and during the work done in this thesis a model for slightly compressible flow was included as an extension of the incompressible flow model. Our code contribution was to further extend the slightly compressible flow model by adding the model equations also considering the temperature, i.e., the energy conservation equation presented in Section 3.1.2.

The code contribution from this work is more specifically an implementation of a semi-implicit and fully coupled model for numerically solving thermal single-phase flow in porous media with the presence of faults. The code is implemented as a Class object in Python with the simulation tool PorePy, and it is developed by use of inheritance of the slightly compressible and incompressible flow model. The concept of inheritance is based on using already existing code, instead of writing all the code from scratch. To give a specific example, the extension from incompressible flow to slightly compressible flow was done by adding support for the time-derivative term in the conservation law presented in Subchapter 3.1. The incompressible flow model already made sure the other two terms were represented in the code, and this relatively small extension was therefore enough to have a model class for solving slightly compressible flow.

5 Simulations, Results and Discussion

This chapter presents code verification and results of the simulations executed in the work of this thesis. Subchapter 5.1 presents the two ways we have verified the code implementation. Subchapter 5.2 and 5.3 presents simulation results in two and three dimensions, respectively, both with and without faults. The simulations show how the temperature deviation from a linear temperature profile varies greatly depending on how high the Rayleigh number is. This linear profile extends from the bottom to the top of the domain and will be referred to as the motionless solution.

For all the visualizations shown we have used the visualization tool ParaView (Ahrens et al., 2005), and within ParaView we have used a filter called *CellDatatoPointData*. According to ParaView's documentation, *vtkCellDataToPointData* is a filter that transforms cell data (i.e., data specified per cell) into point data (i.e., data specified at cell points). The method of transformation is based on averaging the data values of all cells using each point. The actual set of cells attached to the point is used for the averaging process. After the data is transformed to the points, the values in the cell are interpolated linearly. This filter was necessary for computing all the contours presented in this thesis, and Figure 5.1 shows the effect of the filter on a three-dimensional domain. Figure 5.1 a) shows the finite volume solution and the mesh represented in a blue wireframe, while Figure 5.1 b) shows how the solution looks when the filter is applied. Comparing the two figures, one can see that the overall features of the solution remain the same.

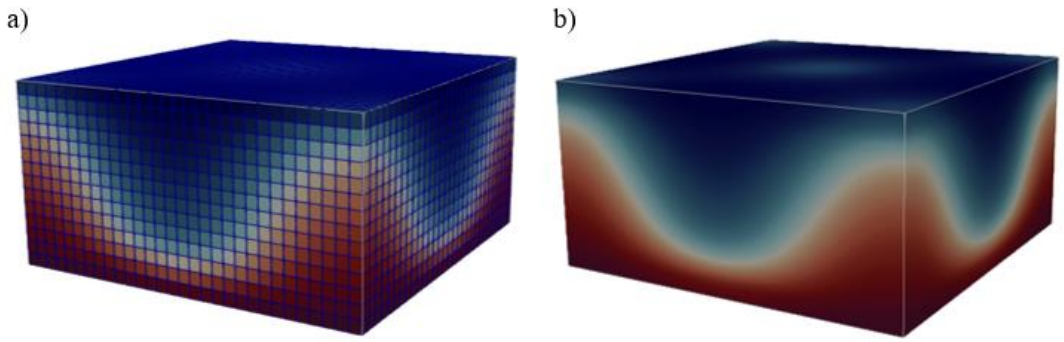

Figure 5.1: a) Domain without the filter CellDatatoPointData applied. Cell edges are kept to clearly show the mesh..b) Domain after the filter CellDatatoPointData has been applied.

All the simulations in this chapter have been performed with cartesian grids because only faults parallel to the axes are considered. We will also mention that all the simulations in this chapter are performed to find the steady state solution. We have checked that steady state is reached by

computing the relative percent difference between the solutions at the two last timesteps in L^2 -norm. For all the simulations this percentage is less than 0.02%.

5.1 Code Verification

5.1.1 Invariance of the Motionless Solution

One of the ways we have verified the code is by checking the consistency of solutions for two different initial conditions. When the simulations are run until steady state, the expected results are that the initial conditions do not alter the steady state solution. The cases we have considered are with a Rayleigh number lower than the critical value, which in turn gives the expectation that any disturbances imposed by an initial condition will diminish. This means that steady state of the simulation is the motionless solution.

Prior to presenting the verification results, we will present the parameters and boundary conditions for the system. We have for all the simulations used parameters representative for conditions in the subseafloor. The parameters are gathered from Zhao et al. (2008) and Schoofs and Hansen (2000), and all of them, except the rock permeability, are presented in Table 5.1. The rock permeability will be specified for each simulation due to this being the parameter we change to vary the Rayleigh number.

Table 5.1: Parameter values for the simulations.

Symbol	Physical parameter	Value	Unit
$\rho_{f,0}$	Fluid reference density	1000	$\mathrm{kg\ m^{-3}}$
ρ_s	Solid density	2600	$\mathrm{kg\ m^{-3}}$
c_f	Fluid specific heat	4185	$\mathrm{J\ kg^{-1}\ K^{-1}}$
c_s	Solid specific heat	815	$\mathrm{J\ kg^{-1}\ K^{-1}}$
Λ_f	Fluid thermal conductivity	0.6	$\mathrm{J\ m^{-1}s^{-1}K^{-1}}$
Λ_s	Solid thermal conductivity	3.35	$\mathrm{J\ m^{-1}s^{-1}K^{-1}}$
β_f	Fluid thermal expansion coefficient	$2.07 \cdot 10^{-4}$	$\mathrm{K^{-1}}$
μ	Fluid viscosity	$1.0 \cdot 10^{-3}$	Pa s
ϕ	Porosity	0.1	–
$\boldsymbol{g}$	Gravitational acceleration	9.81	$\mathrm{m\ s^{-2}}$
$\boldsymbol{K}$	Permeability	–	$\mathrm{m^2}$

The domain we consider is in two dimensions, it measures 2000 m by 1000 m, and has its top at a depth of 1.5 km below sea level. This means that the top is permeable and has a constant pressure. The top is also isothermal, the domain's lateral sides are impermeable and adiabatic, and the bottom is isothermal and impermeable. Details regarding the boundary conditions are shown in Figure 5.2.

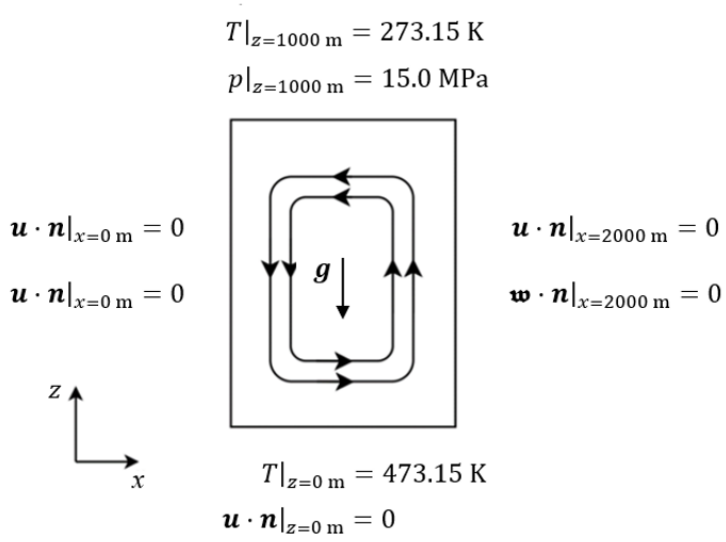

Figure 5.2: Schematic of the boundary conditions.

The initial conditions we are going to use for solution comparison are very different from each other. One of them is imposing a symmetrical and small disturbance, while the other one introduces a larger, asymmetrical disturbance to the system. The symmetrical, small disturbance will be referred to as Initial Condition 1 and will also be used as initial conditions for the results in Subchapter 5.2. The other one is inspired by Yang et al. (1998), and it will be referred to as Initial Condition 2. This initial condition is only for comparison purposes, and will not be used in any further results. Their respective expressions are shown below.

Initial Condition 1:

$$T_0(x,z) = \frac{1000 - z}{5.0} + \frac{\cos\left(\frac{\pi x}{1000}\right)\sin\left(\frac{\pi z}{1000}\right)}{2} + 273.15.$$

Initial Condition 2:

$$T_0(x,z) = \frac{1000 - z}{5}\left(0.5 + \frac{1 - e^{\frac{x-1000}{100}}}{2\left(1 + e^{\frac{x-1000}{100}}\right)}\right) + \left(\frac{1000 - z}{5} - \frac{z(1000 - z)}{5000\, e^{\frac{(200-z)^2}{200\,000}}}\right)\left(0.5 + \frac{1 - e^{\frac{-(x-1000)}{100}}}{2\left(1 + e^{\frac{-(x-1000)}{100}}\right)}\right) + 273.15.$$

Both the initial conditions and the steady state of the system is shown in Figure 5.3 and Figure 5.4. As expected, due to the Rayleigh number being lower than the critical value, the temperature contours even out and result in a linear temperature profile in the end.

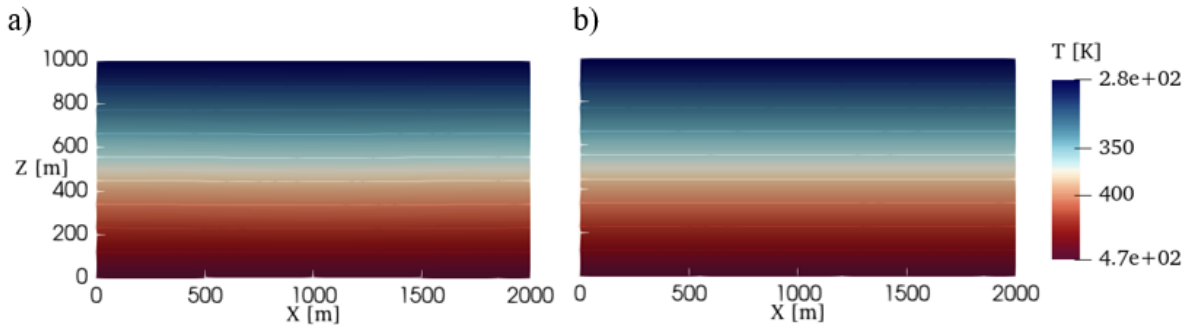

Figure 5.3: a) Initial Condition 1. b) Motionless solution.

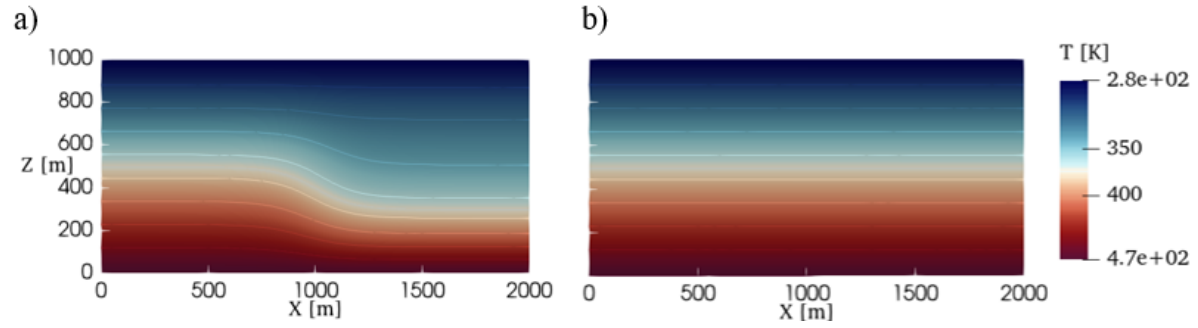

Figure 5.4: a) Initial Condition 2. b) Motionless solution.

This is also checked to hold in three dimensions, but since the results are the same, we have for the sake of brevity left it out of the text.

5.1.2 Verification with Critical Rayleigh Number

In this section a simple methodology to approximate the critical Rayleigh number for three-dimensional cases is presented. All the domains have the horizontal extension $h_h = h_x = h_y$, and the vertical extension is held constant at $h_v = h_z = 1000$ m. The three different domains we have considered in this section hold the following values for the aspect ratio: $\frac{h_h}{h_v} = \left\{\frac{1}{2}, 1, 4\right\}$.

Regardless the initial condition, we look for stationary solutions by enforcing large final simulation time and timestep size. Variations in temperature are quite slow near the critical Rayleigh number, so our choice of large time steps does not induce large errors for finding the motionless solution in a transient manner.

The different horizontal domain extensions, the time parameters, and the non-linear tolerance for the tests in this section is shown in Table 5.2.

Table 5.2: Horizontal domain extensions, time parameters, and non-linear tolerance for critical Rayleigh number verification.

Symbol	Physical parameter	Value	Unit
$h_{h,1}$	Horizontal domain extension	500	m
$h_{h,2}$	Horizontal domain extension	1000	m
$h_{h,3}$	Horizontal domain extension	4000	m
t	Time	50 000 000	Days
Δt	Time-step	500 000	Days
tol	Non-linear tolerance	10^{-6}	–

All the tests in this section employ the boundary conditions presented in Figure 5.2. Initial pressure is a hydrostatic pressure profile, and for the initial temperature we have used Initial Condition 3:

$$T_0(x,y,z) = \frac{1000 - z}{5.0} + \frac{\cos\left(\frac{\pi x}{1000}\right)\cos\left(\frac{\pi y}{1000}\right)\sin\left(\frac{\pi z}{1000}\right)}{10} + 273.15.$$

Moving on to the methodology of this verification, we will recall from Section 5.1.1 that below the critical Rayleigh number, the steady state is the linear, motionless solution, $T_m(x,y,z)$. The numerical scheme used in the code approximates exactly this solution. If we measure the temperature deviation $\Delta T = T(x,y,z,t) - T_m(x,y,z)$ for parameters corresponding to Rayleigh numbers larger than the critical one, we will observe that the solution $T(x,y,z,t)$ deviates from $T_m(x,y,z)$. This means that $\Delta T \neq 0$, which indicates that the convection has been triggered.

To measure the magnitude of ΔT relative to the motionless solution, we introduce the deviation ratio $\delta_T = \frac{\|\Delta T\|}{\|T_m(x,y,z)\|}$ where $\|\cdot\|$ is the L^2-norm over the domain Ω. Due to the numerical scheme in the implementation being able to exactly approximate the motionless solution, the value of δ_T will be numerically zero when the Rayleigh number is below the critical value. Therefore, we will examine the value of both the deviation ratio and the temperature deviation to determine whether convection is occurring.

With what we now know about δ_T and ΔT, we will present how this part of the verification is performed numerically. Figure 5.5 a), Figure 5.6 a) and Figure 5.7 a) present several dots, and each of these individual dots are simulations for different Rayleigh numbers. The spacing of the dots corresponds to a permeability increment of $0.6 \cdot 10^{-14}$ m^2, which in turn causes the Rayleigh number to increase. The value $0.6 \cdot 10^{-14}$ m^2 is chosen arbitrarily and has therefore no theoretical justification.

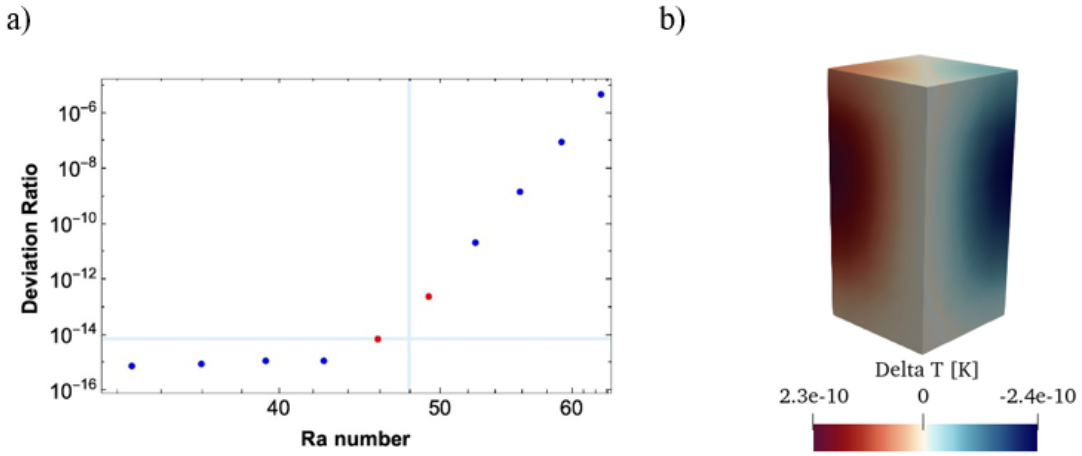

Figure 5.5: Verification case 1 with aspect ratio 0.5. a) Deviation ratio plotted against Rayleigh number where each dot represents an increment in permeability of $\Delta K = 0.6 \cdot 10^{-14}\ m^2$. *Red dots signify the interval* $[45.9,49.2]$ *of which the critical Rayleigh number lies. b)* ΔT *result from Rayleigh number corresponding to* $Ra = 49.2$.

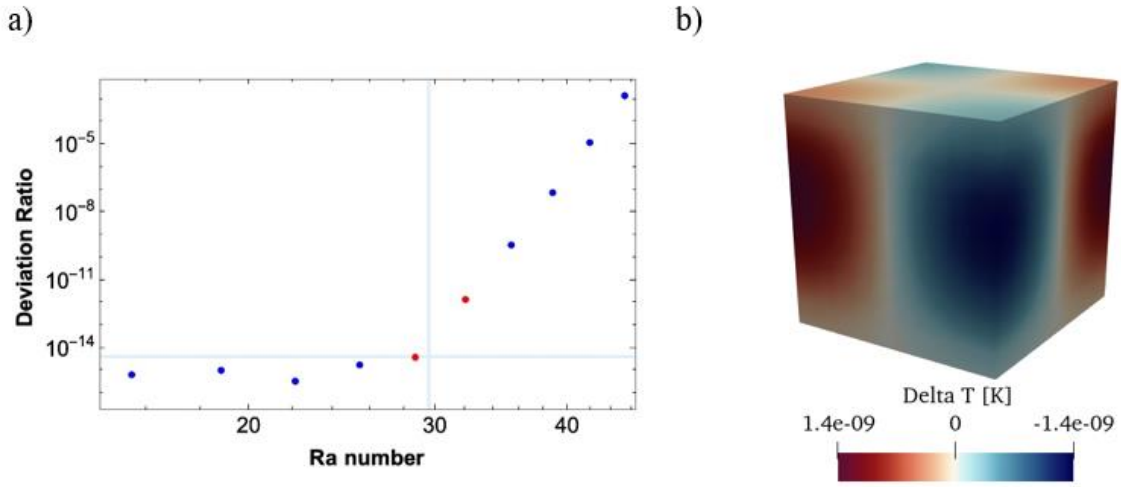

Figure 5.6: Verification case 2 with aspect ratio 1. A) Deviation ratio plotted against Rayleigh number where each dot represents an increment in permeability of $\Delta K = 0.6 \cdot 10^{-14}\ m^2$. *Red dots signify the interval* $[28.7,32.1]$ *of which the critical Rayleigh number lies. b)* ΔT *result from Rayleigh number corresponding to* $Ra = 32.1$.

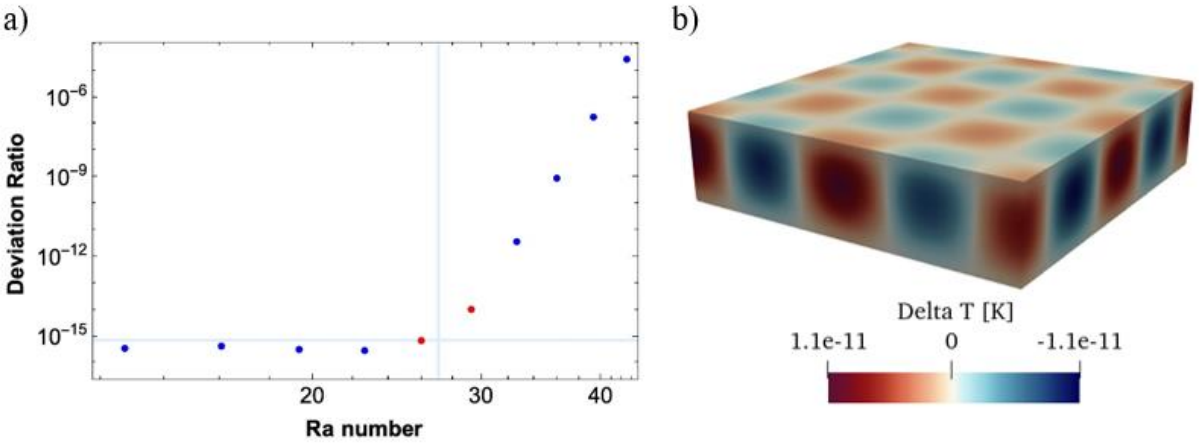

Figure 5.7: Verification case 3 with aspect ratio 4. A) Deviation ratio plotted against Rayleigh number where each dot represents a increment in permeability of $\Delta K = 0.6 \cdot 10^{-14}\ m^2$. *Red dots signify the interval* $[26.0, 29.3]$ *of which the critical Rayleigh number lies. b)* ΔT *result from Rayleigh number corresponding to* $Ra = 29.3$.

For each of the simulations, we computed and visualized the temperature deviation for larger and larger Rayleigh numbers to look for when the square-like convection patterns appear. The first occurrences of convection are shown in Figure 5.5 b), Figure 5.6 b) and Figure 5.7 b), where these results correspond to the Rayleigh number of the right red dot in Figure 5.5 a), Figure 5.6 a) and Figure 5.7 a), respectively. In other words, no convection occurs for simulations corresponding to the left red dot, and convection does occur for simulations corresponding to the right red dot. Therefore, we know that the critical Rayleigh number for the implementation is between the interval created by the two red dots in Figure 5.5 b), Figure 5.6 b) and Figure 5.7 b).

The verification will be completed by comparing the intervals of which we know the critical Rayleigh number of the implementation lies, with theoretical values presented in figure 2 of Tewari and Torrance (1981). This reference presents a figure showing theoretical critical Rayleigh numbers for various aspect ratios, where a ratio equal to 4 gives a critical Rayleigh number of 27.1. Looking to Figure 5.7 a), the critical Rayleigh number is represented by a vertical grid line located at $Ra = 27.1$. We can see that this line goes through the interval we found for the critical Rayleigh number of the implementation.

For the aspect ratios of 0.5 and 1, Tewari and Torrance (1981) do not provide an explicit value of the critical Rayleigh number. Instead, we read from the figure that the critical Rayleigh number for aspect ratios between ≈ 0.9 and ≈ 0.5 is somewhere in the interval $Ra_c = [30, 50]$. Similarly, aspect ratios between ≈ 1.3 and ≈ 0.9 hold critical Rayleigh numbers in the interval $Ra_c = [27.13, 30]$. Here the lower Rayleigh number corresponds to the higher ratio. As the intervals for these theoretical Rayleigh numbers are quite large, we have approximated the critical Rayleigh number corresponding to the ratios we are interested in. This is done by assuming a linear relationship between the theoretical critical Rayleigh numbers and the aspect ratios, and then making an estimate of what the value will be for the ratios 0.5 and 1. Doing this approximation provides us with the approximated theoretical critical Rayleigh numbers of ≈ 47.9 and ≈ 29.6 for aspect ratios 0.5 and 1, respectively. As in the case of an aspect ratio equal to 4 in Figure 5.7 a), we have also visualized the critical Rayleigh numbers of ratios 0.5 and 1 with vertical grid lines in Figure 5.5 a) and Figure 5.6 a), respectively. In these two figures we can see that the vertical grid line, i.e., the critical Rayleigh number, is a member of the Rayleigh number interval created by the two red dots.

By the study we have performed of the critical Rayleigh numbers for the implementation, we will state that the code is consistent with the general claim of Tewari and Torrance (1981) that lower aspect ratios have higher critical Rayleigh numbers. The code is also consistent with the theoretical critical Rayleigh number reported for aspect ratio 4, and the approximated theoretical critical Rayleigh numbers for aspect ratios 0.5 and 1. This can be seen in Figure 5.5 a), Figure 5.6 a) and Figure 5.7 a) by noticing that for each of the ratios, the theoretical critical Rayleigh number is a member of the interval represented by the two red dots.

By this comparison between the theoretical critical Rayleigh numbers from Tewari and Torrance (1981), and the intervals represented by the red dots, we will end this verification chapter.

5.2 Convection in Two-Dimensional Porous Media

In this subchapter we present the two-dimensional simulation results, both with and without faults. For all the simulations in this subchapter, the system has an initial hydrostatic pressure, and Initial Condition 1 which was introduced in Section 5.1.1. The slight disturbance of the linear temperature profile this initial condition introduces will for the simulations regarding higher Rayleigh numbers give us the convection we expect. The parameter values for the rock and fluid used in the simulations are presented in Table 5.1. The only exception is the rock permeability, which will be specified for each simulation due to this being the parameter we are altering to get results for various Rayleigh numbers. Overall CPU-time, simulation time and time-step will be specified in tables for each simulation.

The grid refinement and non-linear tolerance is held constant for every simulation, and for the 2D cases, these parameters hold the values found in Table 5.3.

Table 5.3: Grid refinement and non-linear tolerance for all two-dimensional simulations.

Symbol	Physical parameter	Value	Unit
n_x	Number of cells in x-direction	80	Cells
n_z	Number of cells in z-direction	40	Cells
tol	Non-linear tolerance	10^{-4}	

5.2.1 Without Faults

Recalling the Rayleigh number and its significance for whether convection occurs, we will in this chapter present results from two different simulations considering two greatly different Rayleigh numbers. As already presented in Chapter 1, the critical Rayleigh number for this

problem formulation is bounded below by $Ra_c = 27.1$. Therefore, the simulations we run that have no convection is going to be for Rayleigh numbers lower than 27.1. This way we are certain the steady state solution is the motionless solution.

Convection is essentially all about getting another value for the temperature than "expected", so one can think of the solution with convection as a sum between the systems' motionless solution and some temperature deviations. A procedure for studying convection is to consider these temperature deviations from the motionless, pure conductive, solution (McKibbin, 1986; McKibbin & O'Sullivan, 1980), and we will in the following present how the deviations differ for different Rayleigh numbers. This will be done by subtracting the motionless solution from the solution with convection.

The deviation from the motionless solution will be referred to as the temperature deviation in text, and Delta_T in the figures. We will also show temperature profiles for the overall temperature of the system, and these will be denoted by T in the figures.

The first set of figures to be shown, are the results for a Rayleigh number very close to the critical one. Parameters for this simulation is in Table 5.4.

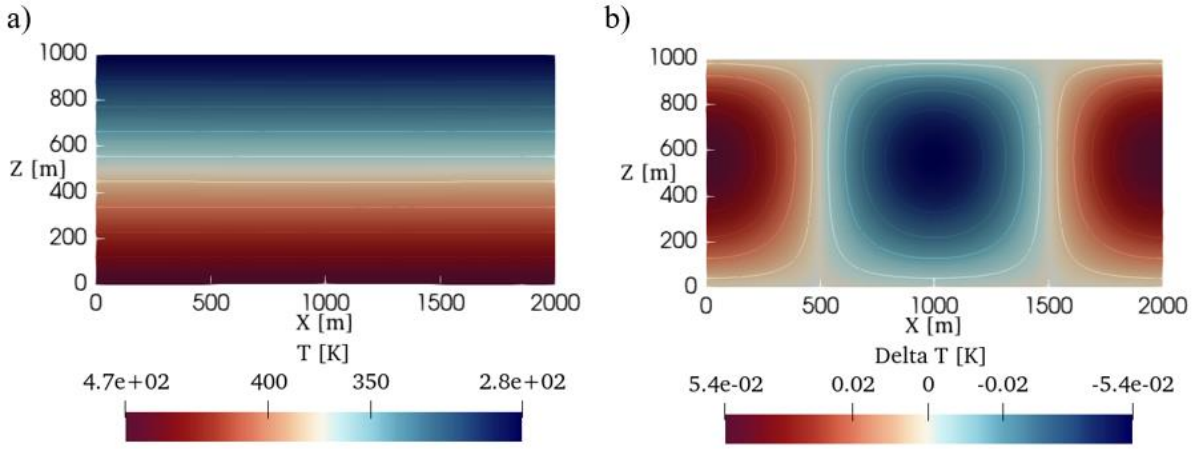

Figure 5.8: Simulation results of convection barely occurring due the Rayleigh number being just above the critical Rayleigh number. a) Shows the temperature profile of the system. b) Temperature deviation from the motionless solution.

In the temperature profile in Figure 5.8 a) one can only barely see the slight dip in some of the temperature contours due to the Rayleigh number being only just above the critical value. If we however look at Figure 5.8 b), there is a clearly visible deviation in the temperature from the motionless solution. Even though it might look like large temperature deviations at first glance, we must refer to the legend to emphasize that the values are in fact quite small.

Table 5.4: Permeability and Rayleigh number for low-Rayleigh number simulation in two dimensions without faults.

Symbol	Physical parameter	Value	Unit
$\boldsymbol{K}$	Permeability	$5.1 \cdot 10^{-14}$	m^2
Ra	Rayleigh number	≈ 28.19	–

Considering a higher Rayleigh number for the simulation gives the expectation of more disturbance in the system, and in turn more visible temperature deviations in the systems' temperature. The simulation results presented in Figure 5.9 will show that a higher Rayleigh number, in this case a value roughly twice of that of the critical value, causes more distorted shapes of the temperature deviation. Parameters for this simulation is presented in Table 5.5.

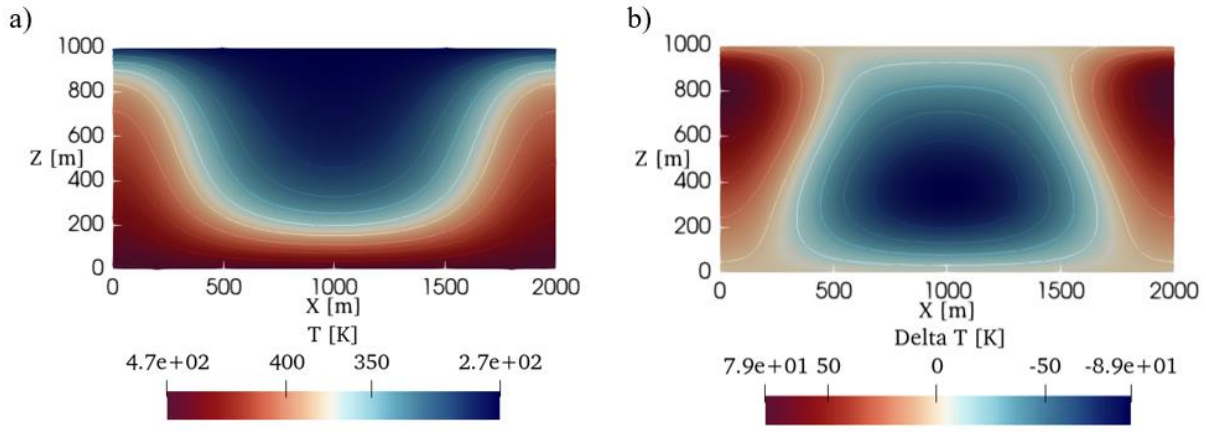

Figure 5.9: Illustrations from a simulation with a high Rayleigh number, and therefore also noticeable convection. a) Temperature contours. b) Temperature deviation from the motionless solution.

The temperature contours presented in Figure 5.9 a) are clearly deviating from the motionless solution, as opposed to those in Figure 5.8 a) where only a very slight dip is to be seen. This can be explained by the drastic increase in the Rayleigh number, which makes the system more unstable and then the convection is more vigorous.

In Figure 5.9 b) one can first notice that the shape of the temperature deviations are a lot more irregular compared to the patterns shown for the lower Rayleigh number in Figure 5.8 b). Having a look at the legend for this figure as well, tells us that the temperature deviations are now a lot larger than before. This signifies that a higher Rayleigh number causes the temperature deviations to be larger than for a lower Rayleigh number. Considering that a doubling in the Rayleigh number causes a thousand times larger temperature deviation from the motionless solution, shows the importance of the Rayleigh number for the convection.

Table 5.5: Permeability and Rayleigh number for high-Rayleigh number simulations in two-dimensions without faults.

Symbol	Physical parameter	Value	Unit
$\boldsymbol{K}$	Permeability	$1.0 \cdot 10^{-13}$	m^2
Ra	Rayleigh number	≈ 55.27	$-$

All the simulations in this section have the parameters for time, grid refinement and nonlinear tolerance shown in Table 5.6.

Table 5.6: Grid refinement and time-parameters for the two-dimensional simulation.

Symbol	Physical parameter	Value	Unit
n_x	Number of cells in x-direction	80	Cells
n_z	Number of cells in z-direction	40	Cells
tol	Non-linear tolerance	10^{-4}	
t	Time	8 000 000	Days
Δt	Time-step	40 000	Days
t_{CPU}	Overall CPU-time	< 1	Minutes

5.2.2 With Faults

Faults present in a rock will make the overall permeability of the system change. In the following simulation cases we have included vertical faults that are more permeable than the host rock both in the tangential and normal direction of the fault. The parameters concerning the host rock is chosen in such a way that the Rayleigh number for the rock is just below the critical value, and therefore no convection is expected in the rock. This section will therefore show what impact the faults have for convection in the system.

Also in this section we compute the result by finding the temperature deviation from the motionless solution. We solve the system for the situation when convection is occurring, and then we subtract the motionless solution from this to check the magnitude of the temperature deviation. This has been done for three different permeability ratios between host rock and the fault, and the permeability values are presented for each of the cases in Table 5.8.

In the faulted cases we have run a simulation for a fault being only 1.5 times more permeable than the host rock. This is what will be considered the motionless solution in this section, and the parameters are shown in Table 5.7.

Table 5.7: Parameters for motionless solution of faulted domain in two-dimensions.

Symbol	Physical parameter	Value	Unit
$\boldsymbol{K}$	Permeability	$4.8 \cdot 10^{-14}$	m^2
$\boldsymbol{K}_l$	Fault permeability (tangential)	$1.5 \cdot \boldsymbol{K}$	m^2
$\boldsymbol{K}_k$	Fault permeability (normal)	$1.5 \cdot \boldsymbol{K}$	m^2
a	Aperture	10.0	m
Ra	Rayleigh number (host)	≈ 26.53	–
t	Time	4 000 000	Days
Δt	Time-step	20 000	Days
t_{CPU}	Overall CPU-time	< 1	Minutes

When we include a fault more permeable than the host rock, it has the expected influence that convection occurs even though the host rock permeability is "too low" for this. Bodvarsson and Lowell (1972) mentions that faults within the rock will cause the fluid to mainly flow through these. Therefore, it is also expected that convection will mainly occur in the fault. In two dimensions, however, this is impossible to see since no convection can occur within a one-dimensional fault. Because of this, the faults will be visualized by a solid white color in the figures presenting results in this section. The expectation regarding convection mainly occurring within the faults will be revisited in Section 5.3.2, which considers convection in faulted, three-dimensional domains.

Moving on to the results for this section, we present Figure 5.10, Figure 5.11 and Figure 5.12 which considers three different fault/host rock permeability ratios. The first figure presents the lowest ratio and the last one presents the highest.

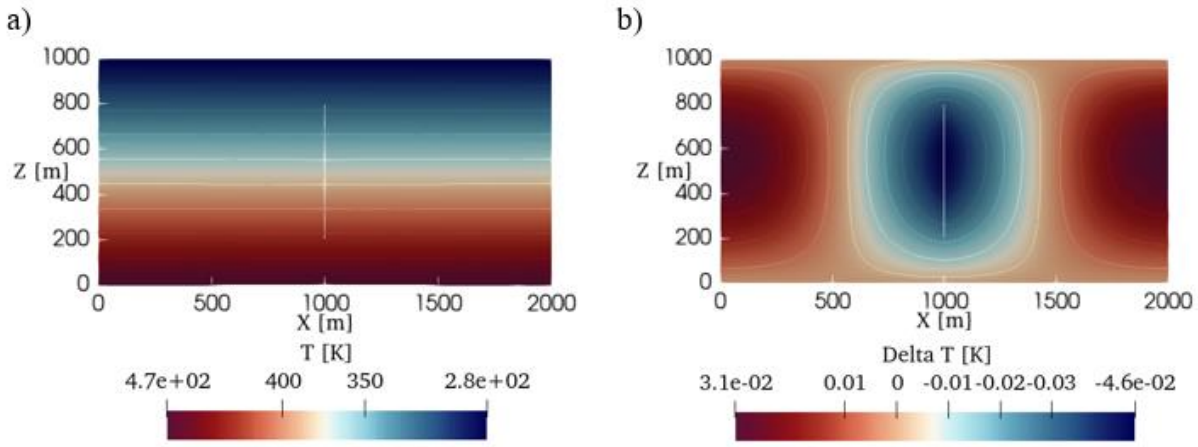

Figure 5.10: Simulation 1/3 with a faulted two-dimensional domain. Corresponding parameter values are denoted by subscript 1 in the parameter table of this section. a) Regular temperature profile. b) Temperature deviation from motionless solution.

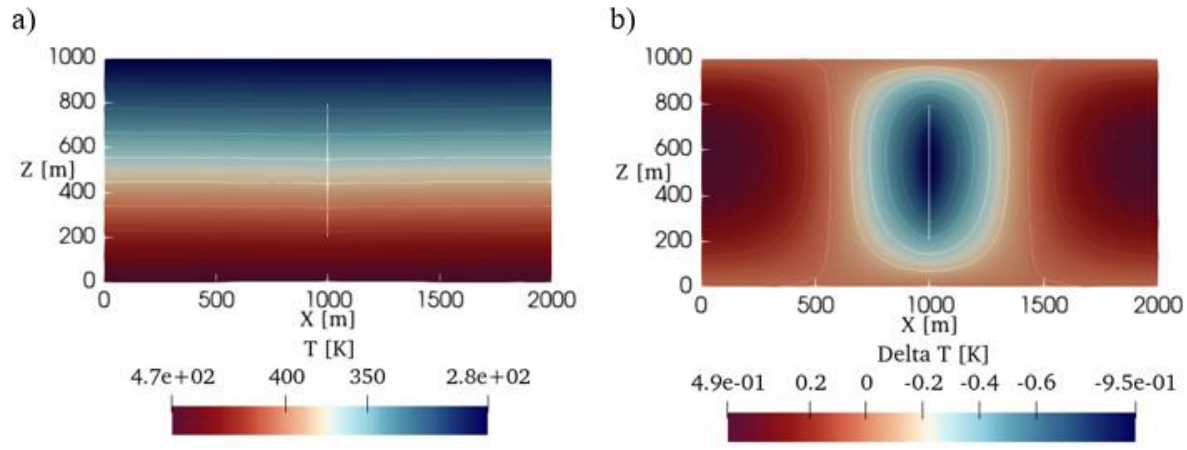

Figure 5.11: Simulation 2/3 with a faulted two-dimensional domain. Corresponding parameter values are denoted by subscript 2 in the parameter table of this section. a) Regular temperature profile. b) Temperature deviation from motionless solution.

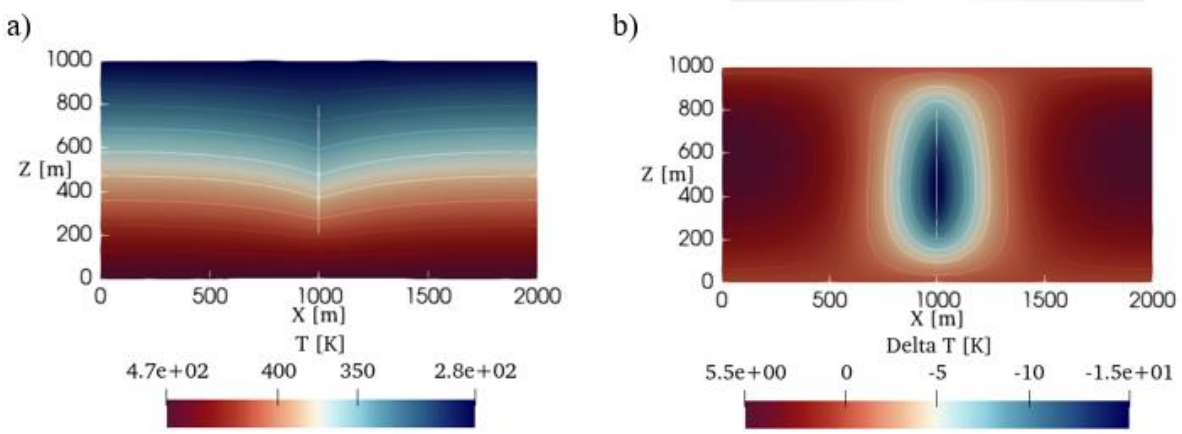

Figure 5.12: Simulation 3/3 with a faulted two-dimensional domain. Corresponding parameter values are denoted by subscript 3 in the parameter table of this section. a) Regular temperature profile. b) Temperature deviation from motionless solution.

Figure 5.10 a), Figure 5.11 a) and Figure 5.12 a) show that the more permeable the fault is, the larger dip there are in the temperature contours. In Figure 5.10 a) the contours seem quite parallel to the x-axis, but as we move to Figure 5.11 a) and Figure 5.12 a) it is more and more visible that the increased fault permeability has an impact. It is therefore clear that higher ratios between the fault permeability and the permeability of the host rock cause the temperature of the system to deviate more from the motionless solution.

For the contours of the temperature deviation shown in Figure 5.10 b), Figure 5.11 b) and Figure 5.12 b), we get the same results as we presented in the previous section: When the system is undergoing more convection, i.e. the Rayleigh number is higher, then the profiles of the temperature deviations get more distorted. For instance, Figure 5.10 b) shows rather regular, square-like shapes for the contours, while Figure 5.11 b) is a lot more distorted.

We will again emphasize that the magnitude of the temperature deviation is varying greatly in the three simulations, as shown in the simulations' respective legends. For the most permeable fault, the system is experiencing a temperature deviation of orders one thousand times larger than for the least permeable fault. This coincides with the results presented by Duwiquet et al. (2019), where they studied temperature anomalies from a motionless solution to a theoretical fault system with one fault for different inclination angles. They investigated these deviations for various permeability ratios for a vertical fault and concluded that the deviations were larger for a higher fault/host rock permeability ratio.

To sum up this section we will state that faults clearly have an impact on convection of a fluid within a porous rock. These simulations consider rocks where the Rayleigh number is too low to expect any convection, which means that a similar domain without a fault just has the motionless solution. However, adding a fault to this system, even if the fault is only one order more permeable, is shown to influence the temperature of the entire system.

Table 5.8: Fault permeabilities and overall CPU-time for the faulted, two-dimensional simulations. Simulation time and time-step is the same as for the motionless solution.

Symbol	Physical parameter	Value	Unit
$\boldsymbol{K}_{l,1}$	Fault permeability (tangential)	$1.0 \cdot 10^{1}\ \boldsymbol{K}$	m^2
$\boldsymbol{K}_{k,1}$	Fault permeability (normal)	$1.0 \cdot 10^{1}\ \boldsymbol{K}$	m^2
t_{CPU1}	Overall CPU-time	< 1	Minutes
$\boldsymbol{K}_{l,2}$	Fault permeability (tangential)	$0.75 \cdot 10^{2}\ \boldsymbol{K}$	m^2
$\boldsymbol{K}_{k,2}$	Fault permeability (normal)	$0.75 \cdot 10^{2}\ \boldsymbol{K}$	m^2
t_{CPU1}	Overall CPU-time	< 1	Minutes
$\boldsymbol{K}_{l,3}$	Fault permeability (tangential)	$0.45 \cdot 10^{2}\ \boldsymbol{K}$	m^2
$\boldsymbol{K}_{k,3}$	Fault permeability (normal)	$0.45 \cdot 10^{2}\ \boldsymbol{K}$	m^2
t_{CPU1}	Overall CPU-time	≈ 1.2	Minutes

5.3 Convection in Three-Dimensional Porous Media

This subchapter will present convection in a three-dimensional porous media, both with and without faults. The domain considered in this subchapter is measuring 2000 m x 2000 m x 1000 m, and a schematic of this can be seen in Figure 5.13.

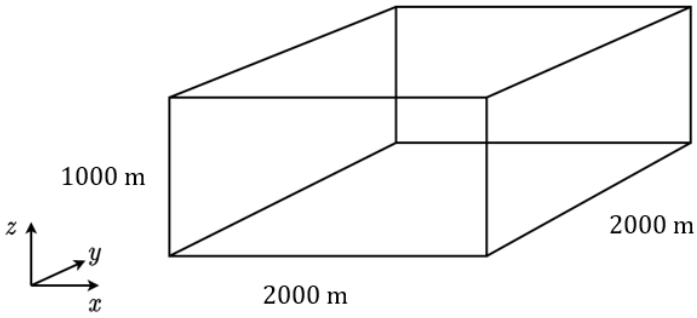

Figure 5.13: Schematic of three-dimensional domain.

Boundary conditions for this case is kept the same as the ones presented for the two-dimensional cases. The only difference is that we now have four lateral sides instead of just two, but all of them follow what applied for the lateral sides in two-dimensions. For details about the boundary conditions, we therefore refer to Figure 5.2, which is shows the boundary conditions for the two-dimensional case.

The initial condition for the pressure is still considered as a hydrostatic pressure profile, but the initial temperature has undergone some changes from the two-dimensional simulations. Initial temperature is now governed by Initial Condition 3 presented in Section 5.1.2

All the simulation parameters of the fluid and rock are held constant for the simulations in this subchapter as well, and they hold the values presented in Table 5.1. The only exception is again the permeability, which will be changed to get results for different Rayleigh numbers. The grid refinement and non-linear tolerance are held constant for all the simulations, and their values are shown in Table 5.9.

Table 5.9: Grid refinement and non-linear tolerance for three-dimensional simulations.

Symbol	Physical parameter	Value	Unit
n_x	Number of cells in x-direction	30	Cells
n_y	Number of cells in y-direction	30	Cells
n_z	Number of cells in z-direction	14	Cells
tol	Non-linear tolerance	10^{-4}	

The way we have moved forward to get the results in this chapter follows the same principle as in the two-dimensional simulations. We compute the temperature deviation from the motionless solution, and then we examine the temperature contours.

5.3.1 Without Faults

This section presents the temperature deviation in a three-dimensional domain without faults. Figure 5.14 and Figure 5.15 show the results for two simulations with different Rayleigh

numbers, where one of them is close to the critical value and the other is further away. Parameters for the two simulations in this section is presented in Table 5.10.

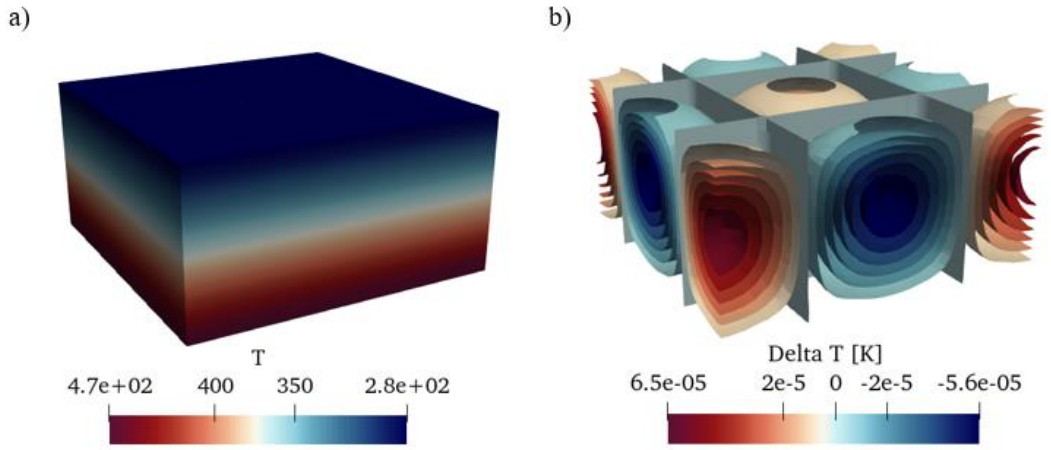

Figure 5.14: Simulation 1/2 in three-dimensional domain. The Rayleigh number is close to the critical value. Values for permeability and Rayleigh number will have subscript 1 in the table at the end of this section. a) Temperature profile, b) Temperature deviation contours from the motionless solution.

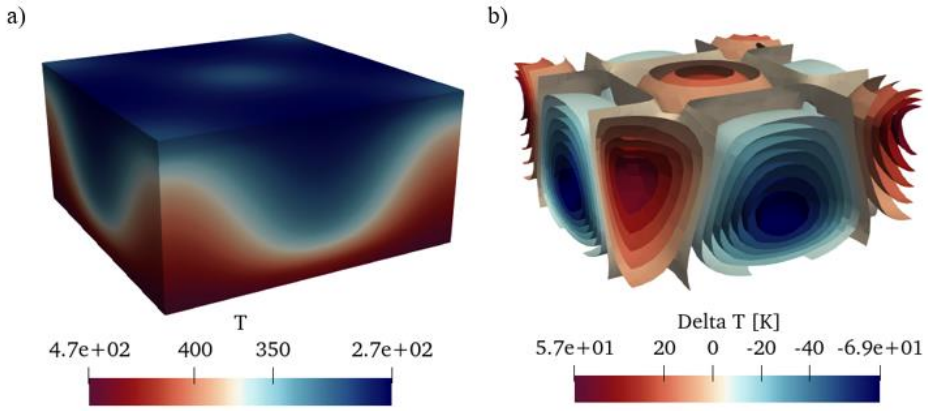

Figure 5.15: Simulation 2/2 in three-dimensional domain. The Rayleigh number is a lot higher than the critical value. Values for permeability and Rayleigh number will have subscript 2 in the table at the end of this section. a) Temperature profile, b) Temperature deviation contours from the motionless solution.

The results in Figure 5.14 and Figure 5.15 are arguably similar to the ones we presented for the two-dimensional case (Figure 5.8 and Figure 5.9). In the same manner it is difficult, if not impossible, to see any deviations in the temperature profiles for the low Rayleigh number shown in Figure 5.14 a). However, for the results corresponding to a higher Rayleigh number in Figure 5.15 a) it is clearly visible that something is going on with the temperature.

We see in Figure 5.14 b) that for a Rayleigh number very close to the critical value, the contours for the temperature deviation have square-like shapes. We also notice that the magnitude of the deviation is very small. For the case of higher Rayleigh number, shown in Figure 5.15 b), the contours have a more irregular shape, and the system has a much larger temperature deviation. In Figure 5.15 b) we see that the shape of the contours is a lot wider at the bottom than at the

top. Hence, in the same way as in the results for the two-dimensional problem, the magnitude of the temperature deviation is larger, and the shape of the contours are more distorted for a higher Rayleigh number.

Table 5.10: Parameters for the three-dimensional simulations without faults.

Symbol	Physical parameter	Value	Unit
$\boldsymbol{K}_1$	Permeability	$5.1 \cdot 10^{-14}$	m^2
$\boldsymbol{K}_2$	Permeability	$1.0 \cdot 10^{-13}$	m^2
Ra_1	Rayleigh number	≈ 28.19	–
Ra_2	Rayleigh number	≈ 55.27	–
t	Time	8 000 000	Days
Δt	Time-step	40 000	Days
t_{CPU}	Overall CPU-time	≈ 13	Minutes

5.3.2 With Faults

As opposed to the results for the faulted domain in two dimensions, it is now possible for us to study convection patterns in the faults. The simulations run here will concern two identical, intersecting faults, whose physical dimensions are a height of 600 m, and a length of 1600 m. The faults are located exactly in the middle of the host rock, making room for 200 m between the fault and the closest domain boundary. For visualizing the location of the faults, we refer to Figure 5.16.

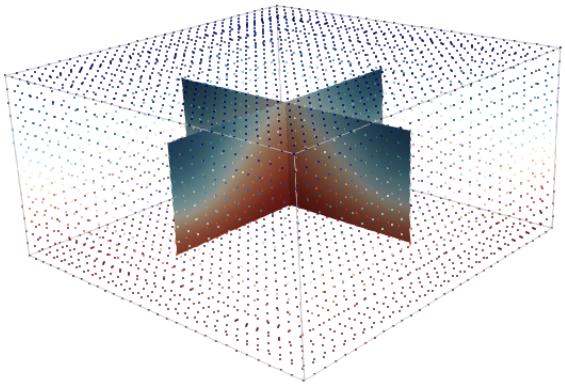

Figure 5.16: Visualization of the fault location within the rock. The rock is here presented only by an outline and points, such that the faults are easier to see.

In Figure 5.17 and Figure 5.18 below we present the first results in this section. The figures show the temperature in a faulted domain with faults very permeable compared to the host rock. The permeability of the host rock is chosen in such a way that the Rayleigh number is below the critical value, and the parameter values for the simulation are presented in Table 5.11.

Table 5.11: Parameters for the three-dimensional simulation with intersecting faults.

Symbol	Physical parameter	Value	Unit
$\boldsymbol{K}$	Permeability (host rock)	$4.8 \cdot 10^{-14}$	m^2
$\boldsymbol{K}_l$	Fault permeability (tangential)	$0.75 \cdot 10^2\ \boldsymbol{K}$	m^2
$\boldsymbol{K}_k$	Fault permeability (normal)	$0.75 \cdot 10^2\ \boldsymbol{K}$	m^2
Ra	Rayleigh number (host rock)	26.53	–
a	Aperture	10.0	m
t	Time	4 000 000	Days
Δt	Time-step	20 000	Days
t_{CPU}	Overall CPU-time	≈ 15	Minutes

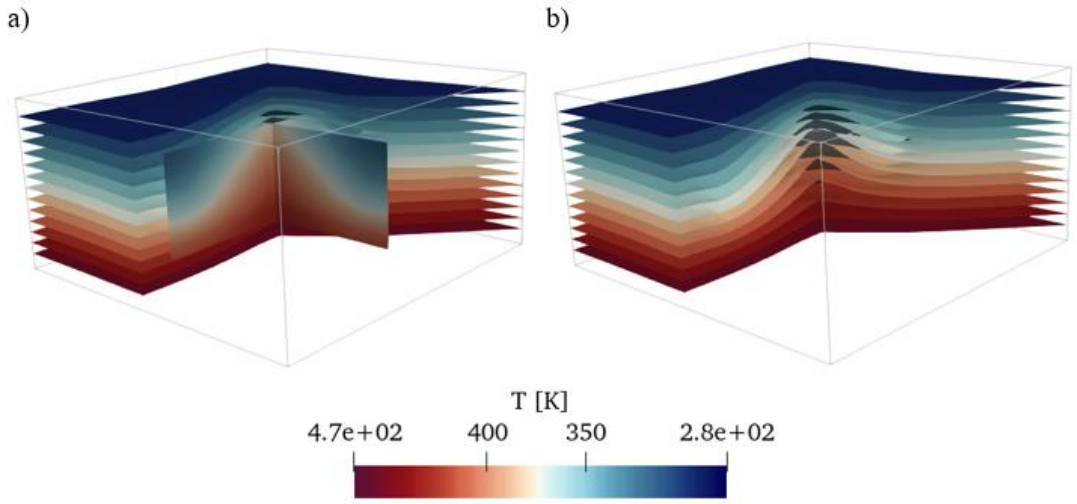

Figure 5.17: Temperature profiles in the rock is presented by fifteen temperature contours ranging from $\approx 273.15\ K$ to $\approx 473.15\ K$. Host rock is clipped such that we can see how the contours are linearly spaced at the corners furthest away from the fault intersection. a) Faults visible. b) Faults hidden.

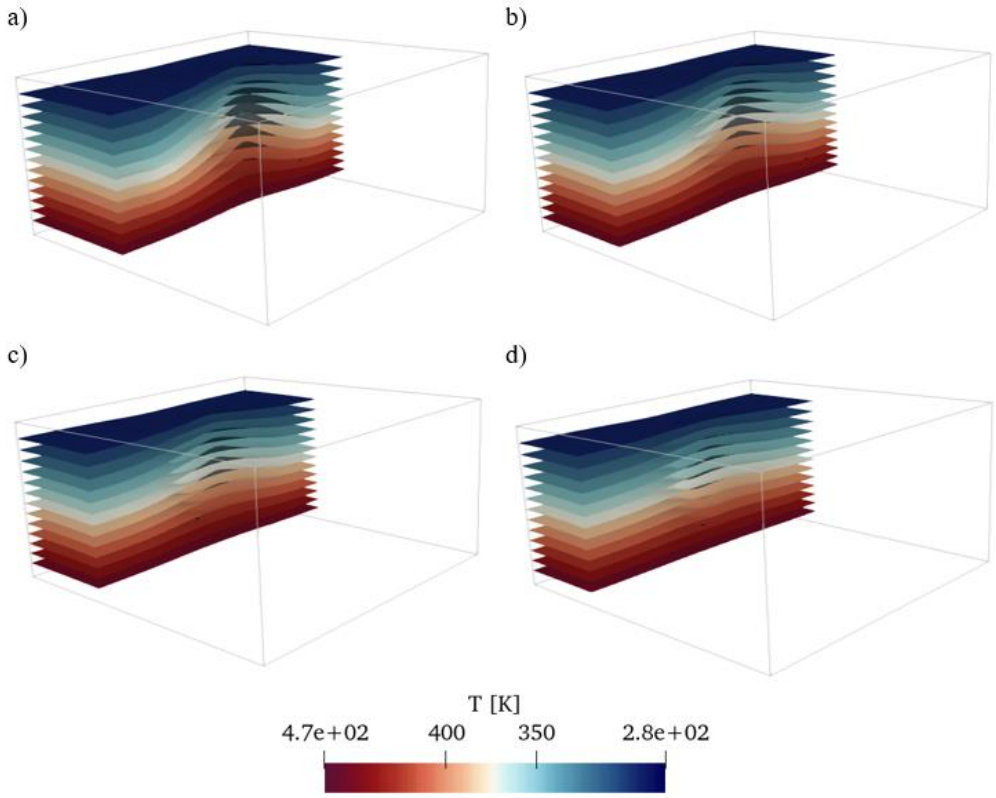

Figure 5.18: Fifteen temperature contours ranging from $\approx 273.15\ K$ *to* $\approx 473.15\ K$ *for simulation of three-dimensional domain with two intersecting faults. The domain is clipped at different locations to show the change in temperature contours with increased distance from the fault intersection. Clipped at: b)* $x = 900$ m, *c)* $x = 800$ m, *d)* $x = 700$ m, *e)* $x = 600$ m.

Figure 5.17 allows us to see the convection patterns within the faults, and to further visualize the effect faults have on the temperature in the rock, we have included Figure 5.18. Figure 5.18 shows how the spatial nonlinearity of the temperature profiles are damped as one gets further away from the fault intersection.

In Figure 5.17 and Figure 5.18 we can clearly see that the temperature has the most prominent changes within the faults. This indicates, as mentioned in Section 5.2.2, that convection occurs mainly in the faults. Due to that Section 5.2.2 only considers one-dimensional faults, there is no convection within the faults since they are only lines. In three dimensions, however, it is clearly visible that the convection patterns are primarily found within the faults, and the temperature of the host rock is influenced because of the fault convection. The host rock itself has parameters corresponding to a subcritical Rayleigh number, but the more permeable faults included to the system still cause visible changes to the temperature throughout the rock. It is therefore likely that the changes in temperature in the rock is due to conductive heat transfer.

Moving on, we will perform a set of similar simulations to those we did in two dimensions, where we studied different permeability ratios between the fault and host rock. Similarly, we

will look further into the temperature deviation from the motionless solution of the system. The motionless solution we are using contains faults being 1.5 times more permeable than the rock, and more details about the parameters for this solution are shown in Table 5.12.

Figure 5.19 and Figure 5.20 shows temperature deviations from the motionless solution for two different simulations. The simulations consider domains with two intersecting faults, where both faults have the same permeability. One of the simulations considers faults being 10 times more permeable than the host rock, and the other considers faults that are 75 times more permeable than the host rock. Expected results are that the temperature deviation is going to have a more regular shape and smaller magnitude for the lower permeability, similar to what we saw in the two-dimensional faulted cases in Section 5.2.2. Parameter values for the three-dimensional faulted simulations are presented in Table 5.13.

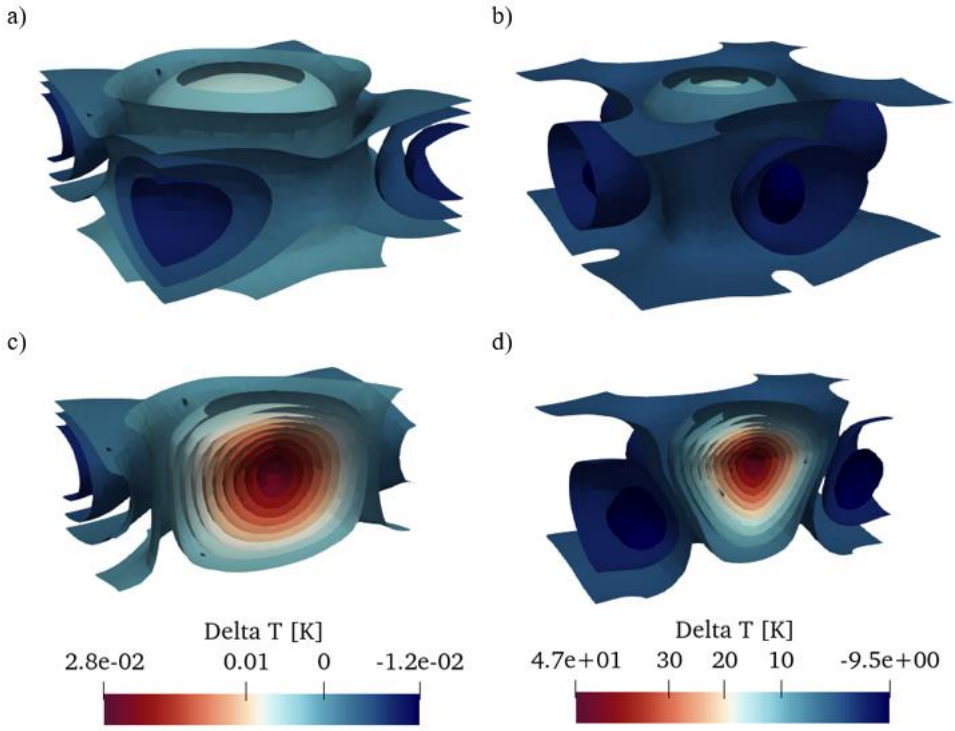

Figure 5.19: Contours for temperature deviation in faulted three-dimensional domains. The domains are clipped in the middle, and the faults are hidden. Figures in the same column correspond to the same case. Columns 1 and 2 have parameters corresponding to subscript 1 and 2, respectively, in parameter table for this section. a) and c) are for the faults 10 *times more permeable than host rock. b) and d) are for the faults* 75 *times more permeable than host rock.*

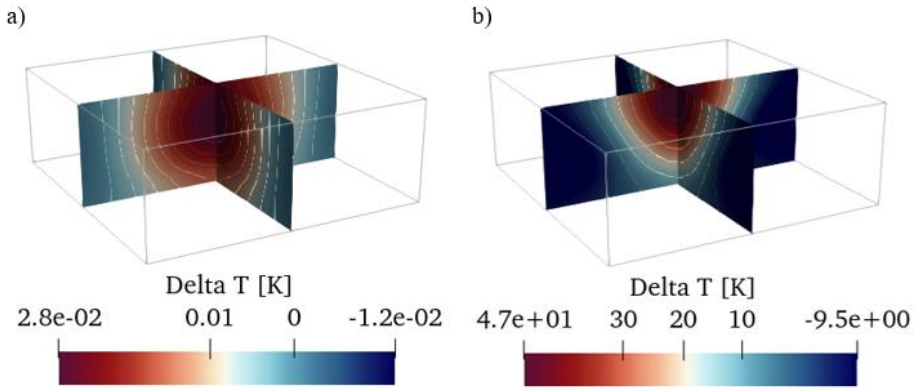

Figure 5.20: Visualization of only the faults. Parameters for a) and b) correspond to those with subscript 1 and 2, respectively, in parameter table for this section. a) Temperature contours within faults 10 times more permeable than host rock. b) Temperature contours within faults 75 times more permeable than host rock.

Figure 5.19 shows the temperature profiles for the entire rock, both clipped and un-clipped, where the clipping is done at the middle of the rock parallel to one of the faults. Figure 5.20 presents the temperature deviation only in the faults. Like the results in two dimensions, we see that the faults with permeability closer to that of the host matrix give more regular profiles for the temperature deviation. Also, the temperature deviation is a lot larger for the faults with permeability furthest away from the rock permeability. This coincides with the expectation that a higher permeability, and therefore a higher Rayleigh number, causes a more vigorous convection where the temperature deviations are larger.

Comparing the results in Figure 5.19 and Figure 5.20 to the low-Rayleigh number case without faults (Figure 5.14) really shows the influence the faults have on the temperature deviations. Where the maximum temperature deviation is of order 10^{-5} for the low-Rayleigh number case without faults, it is of order 10^{-2} and 10^{1} for the lower and higher permeability ratio, respectively, for the faulted case. This is clearly a huge difference, and it shows how much faults matter for convection.

To further investigate the effect of faults, we will compare the significance of a high permeability ($\boldsymbol{K} = 1.0 \cdot 10^{-13}$ m^2) for a rock without faults, to the rock with low permeability containing faults. For the high Rayleigh number case without faults, the temperature deviations have a maximum positive value of just below 60 °C (Figure 5.15). For the faulted case where the host rock has a permeability corresponding to a subcritical Rayleigh number, but with faults having a permeability of almost two orders larger, the maximum positive value of the temperature deviations is just below 50 °C. So, including faults that are more permeable to the system can influence the temperature deviations almost as much as an overall more permeable rock.

Table 5.12: Parameters for motionless, faulted, three-dimensional solution.

Symbol	Physical parameter	Value	Unit
$\boldsymbol{K}$	Permeability (host rock)	$4.8 \cdot 10^{-14}$	m^2
$\boldsymbol{K}_l$	Fault permeability (tangential)	$1.5\ \boldsymbol{K}$	m^2
$\boldsymbol{K}_k$	Fault permeability (normal)	$1.5\ \boldsymbol{K}$	m^2
Ra	Rayleigh number (host rock)	26.53	–
a	Fault aperture	10.0	m
t	Time	4 000 000	Days
Δt	Time-step	20 000	Days
t_{CPU}	Overall CPU-time	≈ 10.5	Minutes

Table 5.13: Values for fault permeability and overall CPU-time for the faulted simulations showing temperature profiles for the temperature differences.

Symbol	Physical parameter	Value	Unit
$\boldsymbol{K}_{l,1}$	Fault permeability (tangential)	$1.0 \cdot 10^1\ \boldsymbol{K}$	m^2
$\boldsymbol{K}_{k,1}$	Fault permeability (normal)	$1.0 \cdot 10^1\ \boldsymbol{K}$	m^2
t_{CPU1}	Overall CPU-time	≈ 10.5	Minutes
$\boldsymbol{K}_{l,2}$	Fault permeability (tangential)	$0.75 \cdot 10^2\ \boldsymbol{K}$	m^2
$\boldsymbol{K}_{k,2}$	Fault permeability (normal)	$0.75 \cdot 10^2\ \boldsymbol{K}$	m^2
t_{CPU1}	Overall CPU-time	≈ 15	Minutes

6 Conclusion

In this thesis we have studied hydrothermal circulation in the subsurface with presence of vertical faults. We have presented a mathematical model for a thermal single-phase flow problem in porous media, where faults were included in the formulation. Inclusion of faults allows for modelling of flow in the presence of discontinuities in the permeability represented by two-dimensional surfaces. Definition of equations, discretization, time stepping, and nonlinear solvers were implemented based on PorePy. The implementation was verified by confirming invariance of the motionless solution, and by benchmarking the implementation against theoretical critical Rayleigh numbers from the literature. The simulations we have shown are the results from solving the fully coupled and semi-implicit hydrothermal model.

This study of convection in porous media has been done by comparing the solution with convection to the solution with only conductive heat transfer, i.e., the motionless solution. Comparisons between these different solutions showed that the shapes of the temperature deviation contours vary greatly with different Rayleigh numbers. It was observed that as Rayleigh numbers increased, the contours got more distorted, and we also observed that the temperature deviations were larger in the more distorted cases.

Convection in a faulted porous rock was also studied by including faults whose permeabilities were larger than that of the host rock. The host rock parameters themselves result in a Rayleigh number too low for any natural convection to occur, but the inclusion of more permeable faults caused onset of convection in the system. The convection mainly happened within the faults due to their higher permeability, but temperature deviations were extended throughout almost the entire host rock. Temperature deviations were larger for faults with higher permeabilities, which is comparable to the results in the absence of faults with a high Rayleigh number. While we cannot be certain how much above the critical Rayleigh number the system is in the faulted cases, more distorted temperature profiles and larger temperature deviations can indicate a Rayleigh number that is significantly higher than the critical value.

7 Bibliography

Ahrens, J., Geveci, B., & Law, C. (2005). ParaView: An End-User Tool for Large Data Visualization. *Visualization Handbook*.

Anderson, M. O. (2018). Deep-sea ore deposits. *Nature Geoscience*, *11*(10), 706-706. https://doi.org/10.1038/s41561-018-0237-y

Beck, J. L. (1972). Convection in a Box of Porous Material Saturated with Fluid. *The Physics of Fluids*, *15*(8), 1377-1383. https://doi.org/10.1063/1.1694096

Berre, I., Boon, W. M., Flemisch, B., Fumagalli, A., Gläser, D., Keilegavlen, E., Scotti, A., Stefansson, I., Tatomir, A., Brenner, K., Burbulla, S., Devloo, P., Duran, O., Favino, M., Hennicker, J., Lee, I. H., Lipnikov, K., Masson, R., Mosthaf, K., . . . Zulian, P. (2021). Verification benchmarks for single-phase flow in three-dimensional fractured porous media. *Advances in Water Resources*, *147*, 103759. https://doi.org/https://doi.org/10.1016/j.advwatres.2020.103759

Bodvarsson, G., & Lowell, R. P. (1972). Ocean-floor heat flow and the circulation of interstitial waters. *Journal of Geophysical Research*, *77*(23), 25-27.

Coumou, D., Driesner, T., & Heinrich, C. A. (2008). The Structure and Dynamics of Mid-Ocean Ridge Hydrothermal Systems. *Science*, *321*(5897), 1825-1828. https://doi.org/10.1126/science.1159582

Courant, R., Isaacson, E., & Rees, M. (1952). On the solution of nonlinear hyperbolic differential equations by finite differences. *Communications on Pure and Applied Mathematics*, *5*(3), 243-255. https://doi.org/https://doi.org/10.1002/cpa.3160050303

Duwiquet, H., Arbaret, L., Guillou-Frottier, L., Heap, M. J., & Bellanger, M. (2019). On the geothermal potential of crustal fault zones: a case study from the Pontgibaud area (French Massif Central, France). *Geothermal Energy*, *7*. https://doi.org/10.1186/s40517-019-0150-7

Fouquet, Y. (2011). Black Smoker. In M. Gargaud, R. Amils, J. C. Quintanilla, H. J. Cleaves, W. M. Irvine, D. L. Pinti, & M. Viso (Eds.), *Encyclopedia of Astrobiology* (pp. 213-213). Springer Berlin Heidelberg. https://doi.org/10.1007/978-3-642-11274-4_201

Géraud, Y., Rosener, M., Surma, F., Place, J., Le Garzic, É., & Diraison, M. (2010). Physical properties of fault zones within a granite body: Example of the Soultz-sous-Forêts geothermal site. *Comptes Rendus Geoscience*, *342*(7), 566-574. https://doi.org/https://doi.org/10.1016/j.crte.2010.02.002

German, C. R., Petersen, S., & Hannington, M. D. (2016). Hydrothermal exploration of mid-ocean ridges: Where might the largest sulfide deposits be forming? *Chemical Geology*, *420*, 114-126. https://doi.org/https://doi.org/10.1016/j.chemgeo.2015.11.006

Graedel, T. E., Harper, E. M., Nassar, N. T., Nuss, P., & Reck, B. K. (2015). Criticality of metals and metalloids. *Proceedings of the National Academy of Sciences*, *112*(14), 4257-4262. https://doi.org/doi:10.1073/pnas.1500415112

Gurtin, M. E. (1981). *An introduction to continuum mechanics*. Academic Press. http://www.loc.gov/catdir/toc/els031/80002335.html

Horton, C. W., & Rogers, F. T. (1945). Convection Currents in a Porous Medium. *Journal of Applied Physics*, *16*(6), 367-370. https://doi.org/10.1063/1.1707601

Huinink, H. (2016). *Fluids in Porous Media*. Morgan & Claypool Publishers. https://doi.org/10.1088/978-1-6817-4297-7

Keilegavlen, E., Berge, R., Fumagalli, A., Starnoni, M., Stefansson, I., Varela, J., & Berre, I. (2021). PorePy: an open-source software for simulation of multiphysics processes in fractured porous media. *Computational Geosciences*, *25*(1), 243-265. https://doi.org/10.1007/s10596-020-10002-5

Kühn, M., & Gessner, K. (2009). Coupled Process Models of Fluid Flow and Heat Transfer in Hydrothermal Systems in Three Dimensions. *Surveys in Geophysics*, *30*, 193-210. https://doi.org/10.1007/s10712-009-9060-8

Lapwood, E. R. (1948). Convection of a fluid in a porous medium. *Mathematical Proceedings of the Cambridge Philosophical Society*, *44*(4), 508-521. https://doi.org/10.1017/S030500410002452X

Martin, V., Jaffré, J., & Roberts, J. (2005). Modeling Fractures and Barriers as Interfaces for Flow in Porous Media. *SIAM J. Scientific Computing*, *26*(5), 1667-1691. https://doi.org/10.1137/S1064827503429363

McKibbin, R. (1986). Thermal convection in a porous layer: Effects of anisotropy and surface boundary conditions. *Transport in Porous Media*, *1*(3), 271-292. https://doi.org/10.1007/BF00238183

McKibbin, R., & O'Sullivan, M. J. (1980). Onset of convection in a layered porous medium heated from below. *Journal of Fluid Mechanics*, *96*(2), 375-393. https://doi.org/10.1017/S0022112080002170

Nordbotten, J. M. (2015). Finite Volume Methods. In B. Engquist (Ed.), *Encyclopedia of Applied and Computational Mathematics* (pp. 545-550). Springer Berlin Heidelberg. https://doi.org/10.1007/978-3-540-70529-1_433

Nordbotten, J. M., & Celia, M. A. (2012). *Geological Storage of CO2: Modeling Approaches for Large-Scale Simulation*. John Wiley & Sons.

Nordbotten, J. M., & Keilegavlen, E. (2021). An Introduction to Multi-Point Flux (MPFA) and Stress (MPSA) Finite Volume Methods for Thermo-poroelasticity. In D. A. Di Pietro, L. Formaggia, & R. Masson (Eds.), *Polyhedral Methods in Geosciences* (Vol. 27, pp. 119-158). Springer.

Patterson, J., & Driesner, T. (2020). Elastic and Thermoelastic Effects on Thermal Water Convection in Fracture Zones. *Journal of Geophysical Research: Solid Earth*, *126*. https://doi.org/10.1029/2020JB020940

Rona, P. A. (1984). Hydrothermal mineralization at seafloor spreading centers. *Earth-Science Reviews*, *20*(1), 1-104. https://doi.org/https://doi.org/10.1016/0012-8252(84)90080-1

Rona, P. A. (2003). Resources of the Sea Floor. *Science*, *299*(5607), 673-674. https://doi.org/doi:10.1126/science.1080679

Rötzer, N., & Schmidt, M. (2018). Decreasing Metal Ore Grades—Is the Fear of Resource Depletion Justified? *Resources*, *7*(4), 88. https://www.mdpi.com/2079-9276/7/4/88

Schoofs, S., & Hansen, U. (2000). Depletion of a brine layer at the base of ridge-crest hydrothermal systems. *Earth and Planetary Science Letters*, *180*(3), 341-353. https://doi.org/https://doi.org/10.1016/S0012-821X(00)00184-9

Stefansson, I., Berre, I., & Keilegavlen, E. (2021). A fully coupled numerical model of thermo-hydro-mechanical processes and fracture contact mechanics in porous media. *Computer Methods in Applied Mechanics and Engineering*, *386*. https://doi.org/https://doi.org/10.1016/j.cma.2021.114122

Stefansson, I., Keilegavlen, E., Halldorsdottir, S., & Berre, I. (2021). Numerical Modelling of Convection-Driven Cooling, Deformation and Fracturing of Thermo-Poroelastic Media. *Transport in Porous Media*, *140*(1), 371-394. https://doi.org/10.1007/s11242-021-01676-1

Tao, C., Seyfried, W. E., Lowell, R. P., Liu, Y., Liang, J., Guo, Z., Ding, K., Zhang, H., Liu, J., Qiu, L., Egorov, I., Liao, S., Zhao, M., Zhou, J., Deng, X., Li, H., Wang, H., Cai, W., Zhang, G., . . . Li, W. (2020). Deep high-temperature hydrothermal circulation in a detachment faulting system on the ultra-slow spreading ridge. *Nature Communications*, *11*(1). https://doi.org/10.1038/s41467-020-15062-w

Tewari, P. K., & Torrance, K. E. (1981). Onset of convection in a box of fluid-saturated porous material with a permeable top. *The Physics of Fluids*, *24*(5), 981-983. https://doi.org/10.1063/1.863472

Yang, J., Latychev, K., & Edwards, R. N. (1998). Numerical computation of hydrothermal fluid circulation in fractured Earth structures. *Geophysical Journal International*, *135*, 627-649. https://doi.org/10.1046/j.1365-246X.1998.00669.x

Zhao, C., Hobbs, B. E., & Ord, A. (2008). *Convective and advective heat transfer in geological systems*. Springer.